Title: Hinge disulfides in human IgG2 CD40 antibodies modulate receptor signaling by regulation of conformation and flexibility

Authors: Christian M Orr, [1,2,3,4,†] Hayden Fisher, [1,2,†] Xiaojie Yu, [2] Claude HT Chan, [2] Yunyun Gao, [3,5,6] Patrick J. Duriez, [2,7] Steven G. Booth, [2] Isabel Elliott, [1,2,8] Tatyana Inzhelevskaya, [2] Ian Mockridge, [2] Christine A. Penfold, [2] Armin Wagner, [4] Martin J. Glennie, [2] Ann L. White, [2,9] Jonathan W. Essex, [8,10,‡] Arwen R. Pearson, [3,5,‡] Mark S. Cragg, [2,10,‡] Ivo Tews, [1,10, ‡,*]

Affiliations:

[1]University of Southampton, Biological Sciences; Southampton SO17 1BJ, UK.

[2]University of Southampton, Centre for Cancer Immunology; Southampton, SO16 6YD, UK.

[3]Hamburg Centre for Ultrafast Imaging CFEL; Hamburg 22761, Germany.

[4]Diamond Light Source; Didcot, OX11 0FA, UK.

[5]Institute for Nanostructure and Solid State Physics; Hamburg 22761, Germany.

[6]Max Planck Institute for the Structure and Dynamics of Matter; Hamburg 22761, Germany.

[7]University of Southampton, CRUK Protein Core Facility; Southampton, SO16 6YD, UK.

[8]University of Southampton, School of Chemistry; Southampton SO17 1BJ, UK.

[9]UCB Pharma; Slough, SL1 3WE, UK.

[10]University of Southampton, Institute for Life Sciences; Southampton SO17 1BJ, UK.

*Corresponding author. Email: ivo.tews@soton.ac.uk

†These authors contributed equally

‡Senior authors

Abstract: Antibodies protect from infection, underpin successful vaccines and elicit therapeutic responses in otherwise untreatable cancers and autoimmune conditions. The human IgG2 isotype displays a unique capacity to undergo disulfide shuffling in the hinge region, leading to modulation of its ability to drive target receptor signaling (agonism) in a variety of important immune receptors, through hitherto unexplained molecular mechanisms. To address the underlying process and reveal how hinge disulfide orientation affects agonistic activity we generated a series of cysteine to serine exchange variants in the hinge of the clinically relevant monoclonal antibody ChiLob7/4 directed against the key immune receptor CD40 were used to test how hinge disulfide formation affects agonistic activity. We report how agonistic activity, independently of epitope, varies with disulfide pattern, and is afforded by the presence of a disulfide cross-over between F(ab) arms in the agonistic forms as observed in the determined crystallographic structures. This structural "switch" impacts directly on antibody conformation and flexibility. Small-angle X-ray scattering and ensemble modeling demonstrated that the least flexible variants adopt the fewest conformations and evoke the highest levels of receptor agonism. This covalent change may be amenable for broad implementation to modulate receptor signaling in an epitope-independent manner in future therapeutics.

One Sentence Summary: Covalent disulfide switching in the hinge region of human IgG2 CD40 antibodies provides a model for antibody conformational regulation.

Main Text:

INTRODUCTION

Monoclonal antibodies (mAb) are an increasingly important therapeutic modality, representing ~eighty percent of therapeutic biologics (*1*). They continue to translate into the clinic and by May 2021, the FDA had approved 100 antibody drugs (*2*), with a strong upward trend (*3*). This success represents their dual ability to bind diverse targets with exquisite specificity and leverage powerful immune effector functions *(4)*. Target binding is mediated through two identical fragment antigen-binding (F(ab)) domains which are linked through a hinge to the fragment crystallizable (Fc) domain. The Fc portion elicits immune effector mechanisms that can be influenced by choice of isotype: human (*h*) *h*IgG1 and *h*IgG3 are powerful activators of the complement cascade and Fc gamma receptor (FcγR) expressing cells, while *h*IgG2 and *h*IgG4 are more inert *(5)*. Properties of the Fc can be further engineered to modulate pharmacological activity (*6, 7*). Antibodies can also evoke potent effector mechanisms when the F(ab) portions bind cell surface receptors on immune cells *(8)*. Prominent targets include immune receptors of the Tumor Necrosis Factor Receptor Super-Family (TNFRSF) (*9*). CD40 is one such receptor, essential for initiation and regulation of adaptive immunity *(10)*. CD40 immunostimulatory mAb can mimic endogenous CD40 ligand, providing powerful curative anti-tumor effects in mouse models *(11)*.

Several studies performed to date have shown that mAb activity typically depends upon both the epitope recognized and the isotype (reviewed in (*12*)). Very rare antibodies such as the powerful agonist anti-CD40 mAb CP870,893 appear highly agonistic in any isotype (*13*), presumably reflecting a specific binding epitope. With respect to human isotypes, we previously demonstrated for CD40 that of the four human isotypes, *h*IgG2 afforded the strongest agonism, including with two clinically relevant anti-CD40 mAb, SGN-40 and ChiLob7/4 (*13*). This same effect was also observed in an entirely different receptor family with *h*IgG2 shown to be the optimal isotype for stimulating CD28, a member of the immunoglobulin super family (*13*), and in a wider panel of clinically relevant anti-CD40 agonistic mAb (*14*). Subsequently we showed that the *h*IgG2 isotype was even capable of converting antagonistic CD40 ligand-blocking antibodies into powerful agonists (*15*). We recently broadened these observations to two additional therapeutically exciting TNFRs, namely 4-1BB and OX40 (*16*), showing that the *h*IgG2 isoform drives greater receptor clustering and activity across multiple TNFR family members.

Uniquely, the *h*IgG2 hinge can undergo disulfide-switching resulting from natural redox processes in the blood (*17, 18*). During this process, disulfide bonds between two cysteines can be broken and re-formed with an alternative cysteine at a different position. While disulfide connectivity has been investigated before (*19*), the exact topology and relationship to biological properties remained unknown. Two isoforms, described as the A-form (*h*IgG2A) and the B-form (*h*IgG2B), are thought to represent the two extremes of this process. While the evolutionary basis and functional consequences of this switching are debated *(17-19)*, it is known that *h*IgG2 is the major isotype produced against bacterial carbohydrates in response to infection (*20*). For CD40-targeting mAb, the two isoforms have starkly contrasting immunostimulatory activity: *h*IgG2A is inert, devoid of stimulatory activity, while *h*IgG2B is strongly agonistic (*13, 14*).

Given our previous observations that the activity of anti-CD40 and other immunostimulatory mAb can be augmented through interaction with FcγRs and the inhibitory FcγRIIB in particular

(*14, 21-23*), the agonistic activity of *h*IgG2 was surprisingly shown to be FcγR-independent. In experiments using mouse dendritic cells (DC) or B cells expressing human CD40, human B cells (*13-15*), as well as FcγR knock-out mice and employing Fc mutants with impaired FcγR interactions (N297Q, N265A, C4d), activity was retained both *in vitro* and *in vivo* in the absence of FcγR involvement. Critically, the retained activity of $F(ab)_2$ fragments demonstrated *de facto* Fc-independent biological activity associated with the *h*IgG2 hinge (*13*). These observations are in opposition to the prevailing model that epitope recognition differentiates agonistic antibody function alongside FcγR engagement.

Hinge-conferred agonistic activity currently lacks a satisfactory mechanistic explanation. We therefore studied the effect of hinge variation in the clinically relevant anti-CD40 mAb ChiLob7/4 (*13*). We used a combination of biological activity assays, structural/biophysical analyses and computational methods to show that disulfide switching in the hinge region alters mAb flexibility and conformational dynamics, thus affecting mAb agonistic activity. Hinge variation thus controls antibody function and provides an opportunity for targeted engineering to control immunostimulatory activity in future antibody therapeutics.

RESULTS

Disulfide hinge variation alters the biological activity (agonism) of mAb

To investigate the effect of the hinge region on mAb agonistic activity, we generated a series of six $F(ab)_2$ variants of the anti-CD40 antibody ChiLob7/4. Cysteines in the hinge region proposed to be involved in disulfide shuffling were exchanged to serine. Both single (C233S, C232S, C239S) and compound dual cysteine to serine exchange variants (C/S) were generated (C232S+C233S, C233SκC214S, C232SκC214S; NB: κ indicates kappa light chain). Whole IgG was produced, prior to pepsin digestion to generate $F(ab)_2$ fragments, which were then purified and evaluated for their Fc-independent agonistic activity (see Methods).

Activity was first assessed using transgenic mouse B cells that express *h*CD40. We employed three complementary assays established previously (*13, 14*) that provide cellular read-outs of homotypic adhesion (cell:cell clustering), activation (upregulation of CD23) and proliferation *(24)*. We have observed good concordance between these assays and activities on DC and *in vivo* expansion of antigen-specific CD8 T cells, with associated therapeutic impacts (*13-15, 25*). As a negative control and comparator for our anti-*h*CD40 ChiLob7/4 *h*IgG2 C/S variants we used the parental mAb ChiLob7/4 in a *h*IgG1 isotype, previously shown to have minimal agonistic activity (*13, 14*). As a positive control we used CP870,893 *h*IgG1, which we previously showed is highly agonistic in any isotype (*13, 14*).

Flow-cytometric analysis shown in **Fig. 1A** reveals that CD23 upregulation varied markedly across the variants. C232S+C233S was inert, akin to the ChiLob7/4 *h*IgG1 negative control, while C232SκC214S activity approached that of the highly agonistic CP870,893 positive control (*13, 14*). Homotypic adhesion, indicated by the appearance of densely packed dark regions in **Fig. 1B**, was absent from the agonistically inert ChiLob7/4 *h*IgG1 negative control as well as C232S+C233S and C233S, but was evident in other variants, most notably C239S and C232SκC214S. Increased ^{3}H-thymidine incorporation corresponding with higher proliferation rates *(26)* was highest in the C239S and C232SκC214S variants, as shown in **Fig. 1C**.

The data were largely consistent across all three assays and distinguish inert C/S variants from stronger agonists, though differences in the order were observed. C/S variants C232S+C233S,

C233S and C232S displayed indiscriminate levels of CD23 upregulation, but showed small differences in proliferation and homotypic adhesion. Similarly, while C232SκC214S appeared to be as potent as CP870,893 in triggering upregulation of CD23, it did not elicit equivalent proliferation, **Fig. 1**. We assume these examples reflect the differences in signaling threshold required to elicit the varying cellular outputs. Where discrepancies occurred, we took proliferation as the key cellular output in ascribing relative levels of CD40 agonism to the C/S variants, allowing for an ordering of variants by increasing agonistic activity as C232S+C233S ≅ C233S < C232S < C233SκC214S < C239S ≅ C232SκC214S.

To confirm the activity hierarchy in a wider set of cellular assays, we made use of a *h*CD40-expressing human Jurkat-NFκB-GFP reporter line (*16*) in which GFP is produced in response to NFκB activation after *h*CD40 engagement. Taking the most inert ChiLob7/4 *h*IgG2 C/S variant (C232S+C233S), the most active (C232SκC214S), and an intermediate (C233SκC214S) C/S variant, alongside *h*IgG1 (-) and *h*IgG2 (+) controls, we showed that the activity hierarchy remained the same for both $F(ab)_2$ fragments and full IgGs (**Fig. S1A**). We subsequently evaluated the same variants on purified human B cells, assessing B cell activation (upregulation of major histocompatibility complex II; MHCII), adhesion and proliferation, as above. Flow-cytometric analysis (**Fig. S1B**) revealed that MHCII upregulation increased from *h*IgG1 and *h*IgG2 C232S+C233S, to C233SκC214S, being highest with C232SκC214S. Homotypic adhesion was absent from the agonistically inert ChiLob7/4 *h*IgG1 negative control and the C232S+C233S variant, and was most evident after stimulation with the C232SκC214S variant, as expected (**Fig. S1C**). Increased ^{3}H-thymidine incorporation (**Fig. S1D**) reflected these changes and corresponded with the previously established hierarchy.

All mAb variants tested have identical F(ab) regions and thus are predicted to bind equivalently to the same epitope on *h*CD40. However, it remained possible that hinge C/S differences might still result in altered affinity. To evaluate this, we performed surface plasmon resonance (SPR), selecting the non-agonist variant C232S+C233S, the modest agonist C233SκC214S, and the strong agonist C232SκC214S alongside the parental *h*IgG2 as a control, and tested all variants in both IgG and $F(ab)_2$ formats. All formats and variants retained similarly high affinity to *h*CD40 (**Fig. S1E** and **Table S1**). This was confirmed in cell binding studies using both *h*CD40-expressing Jurkat cells and naturally *h*CD40-expressing Ramos B cells. Cell binding was retained in all variants as anticipated, with slightly higher binding for the non-agonistic C232S+C233S variant (**Fig. S1F**). Having further characterized the C/S variants and confirmed their activity hierarchy across multiple readouts and cell-types, we undertook to evaluate the underpinning mechanistic explanation.

Crystal structures reveal a disulfide cross-over in agonistic mAb

Native *h*IgG2 antibodies are predicted to possess stabilizing disulfides between heavy and light chains. Typically, disulfides are expected to occur in the hinge region connecting the two heavy chains at C232, C233, C239 and C242; additionally, heavy and κ light chains are linked by a disulfide between heavy chain C127 and κ light chain C214 (**Fig. 2A**). All ChiLob7/4 C/S variants had identical variable regions, and so any change in activity would solely depend on their ability to form disulfides at the hinge region with potential impacts on structure. To evaluate this, we sought to determine the structure of their $F(ab)_2$ fragments using X-ray crystallography. The structures of the $F(ab)_2$ variants revealed similar overall conformation,

though two crystal forms were observed, with the C232S variant favoring a slightly more extended conformation (**Fig. S2**).

As antibody hinge regions are difficult to observe in crystal structures due to their natural flexibility *(27)*, an anomalous scattering approach was used to reveal the disulfide connectivity of the F(ab)$_2$ fragments. Performing structure determination at an X-ray wavelength where significant anomalous scattering for sulfur atoms was observed (*28*) enabled the determination of sulfur positions (**Table S2** and **Fig. S3**), and thus enabled us to resolve hinge disulfide topology. The disulfides between the two C239 side chains or the two C242 side chains were not resolved in electron density in any of the structures indicating flexibility in this region; shown as dashed lines in **Fig. 2B**.

In the non-agonistic variants C232S and C233S the C127-κC214 disulfide between heavy and light chains is confirmed, **Fig. 2B**. Additionally, the C232S variant resolves the disulfide between the two C233 residues on opposite heavy chains (while the two C232 residues in the non-agonist C233S are not resolved). In contrast, in the C232S+C233S double variant neither disulfide can form; hence this variant may have higher inherent hinge flexibility, which may explain failure to yield diffraction quality crystals (see Methods).

Surprisingly, structures of agonistic variants lack the C127 to κC214 disulfide that stabilizes the association between the light and heavy chain. The interface between light and heavy chain buries an interface area of ~1700 Å^2, and is predicted to form with a ΔG -24.8 kcal/M and a binding energy of -32.2 kcal/M as determined using PISA (*29*), suggesting strong association of heavy and light chain, even in the absence of the stabilizing disulfide. However, the heavy chain C127 instead engages in a cross-over to the opposing heavy chain in the hinge. This in turn prevents the formation of C232 or C233 paired disulfides. In the highly agonistic C232SκC214S and C239S the cross-over forms between C127 and C233, **Fig. 2B**. In the weakly agonistic C233SκC214S, the disulfide cross-over forms between C127 and C232. Together these data demonstrate that despite large similarities in overall structure, the disulfide patterns were markedly different across the variants, with a disulfide cross-over present in agonistic mAb.

Disulfide cross-over in the *h*IgG2 hinge restricts mAb conformation

The cross-over variants, C233SκC214S, C239S and C232SκC214S, were agonistic with some variation in biological activity, **Fig. 1**. We hypothesized that disulfide cross-over drives agonism by conformational restriction. We therefore used small-angle X-ray scattering (SAXS) to study conformational states in solution-phase. Primary analysis of the SAXS data showed trends in the R_g and D_{max} that correspond with activity (**Table S3**).

The P(r) analyses of SAXS data (*30*) revealed maximum dimensions (D_{max}) of particles in solution ranging from 132.5-137 Å for the agonistic cross-over variants C233SκC214S, C239S and C232SκC214S, **Table S3**. The less agonistic variants C232S+C233S, C233S and C232S were less compact (D_{max} values ranging from 142-150.5 Å). This same trend was seen in the natural isoforms where agonistic *h*IgG2B was retarded in size exclusion chromatography, compared with non-agonistic *h*IgG2A (*17, 18*). Consistently, the data suggest that a more compact structure corresponds to agonism.

The dimensionless Kratky plot (*31*) was used to compare the F(ab)$_2$ C/S variants. In this plot, an ideal globular protein would result in a Gaussian peak at the Guinier-Kratky point, shown as a grey crosshair in **Fig 3**. Owing to the elongated shape of F(ab)$_2$ fragments, all variants showed

deviation from this Gaussian distribution, with the degree of deviation corresponding with activity. The least agonistic variant C232S+C233S showed the greatest deviation, while the most agonistic variant C232SκC214S was much closer to a Gaussian, (red and blue datasets, respectively, in **Fig 3**). The remaining variants fell between these two extremes. This behavior can be explained by a more extended structure or a greater flexibility in solution for the non-agonistic variants compared to agonistic variants. Notably, the C232S+C233S double variant (which is unable to form either the C232-C232 or C233-C233 disulfides) shows the largest deviation, with the difficulty of crystallizing this variant supporting higher flexibility.

To study the conformation, the crystal structures were fit against their corresponding SAXS data (**Table S3**). For this analysis, amino acids unresolved in electron density and missing from the crystallographic models were added (blue line in **Fig. S4**). Rigid body normal mode refinement using SREFLEX (*32*) was attempted using standard parameters but failed to correctly define domains due to the complexity of the disulfide cross-overs. The fit was improved when the hinge region was removed and each F(ab) arm was treated as one domain, whereby χ^2 fits < 2 were achieved (orange line in **Fig. S4**). However, SREFLEX is not able to model structural flexibility as an ensemble of conformations, which was suggested from the dimensionless Kratky plot as being present to varying degrees in all C/S variants. Together, these data demonstrated that the C/S variants exhibit differing behaviors in solution, with the agonistic variants associated with more compact conformations. Next, their flexibility was assessed.

Agonistic variants have a less diverse pool of conformations

To appropriate the flexibility of the $F(ab)_2$ C/S variants, we utilized a combination of SAXS and molecular dynamics (MD) simulations (*33*). Rather than the rigid body fit described above, this approach gives access to a conformational pool that accurately defines the restraints imposed by the complex disulfide bonding patterns at the hinge as determined from the crystal structures. Atomistic molecular dynamics combined with a reweighting approach is a well-established method for such analyses (*34*).

A conformational pool of 8000 structural states for each variant was generated by atomistic MD, which was then explored with ensemble fitting using GAJOE (*35*). Structures from the pool were reweighted using the experimental SAXS data to bias the distribution and represent the solution-phase conformations. Both the MD generated pool of conformations and the SAXS reweighted ensembles show a tightening of the R_g distribution for agonistic *h*IgG2 variants, with non-agonistic variants sampling a more conformationally diverse pool of structures, **Fig. 4A**. The analysis reveals that variation in the pool of models is much larger in non-agonistic variants compared to agonistic variants. The R_{flex} parameter (*36*) in GAJOE can be used to quantify system flexibility, where 100% indicates maximal flexibility, and 0% represents a rigid structure. The non-agonistic variants exhibit R_{flex} values of ~90%, indicating high flexibility, whereas agonistic variants have R_{flex} values between 55% and 70%, indicating reduced flexibility (**Table S3**).

The fit of ensembles against corresponding SAXS data showed good agreement in residual plots, **Fig. 4B** (black line in **Fig. S4**) and revealed several trends consistent with activity (**Table S3**). Non-agonistic variants displayed conformation sampling over a greater range of R_g and D_{max} values compared to agonists while agonistic variants sampling a smaller range of R_g and D_{max} values provided an optimal fit to the SAX data. This highlights that the non-agonistic variants display greater flexibility than the agonistic variants. Also informative was analysis of hinge and

torsion angles between the two F(ab) arms (defined in **Fig. S5**) of representative models from the systems, where a strong trend was seen with non-agonists showing the greatest variance (**Table S3**). These observations are consistent with non-agonistic variants having a greater degree of conformational flexibility compared to agonists. Thus, agonist activity is reflected not only in more compact structures, but critically also in decreased flexibility.

DISCUSSION

Since native signaling by TNFRs requires ligand-induced receptor trimerization and higher-order receptor clustering *(16, 37, 38),* agonistic antibodies likely mimic this natural activation process. For anti-CD40 mAb, agonism is directly associated with receptor clustering (*15, 16*). We show here that the presence of a disulfide cross-over in *h*IgG2 variants corresponds with increased agonistic activity, **Fig. 1** & **Fig. 2**. The specific hinge structure limits $F(ab)_2$ flexibility and controls conformational freedom, as revealed by the dynamic properties seen in solution and by MD analysis, **Fig. 3** & **Fig. 4**. Consequently, we predict that cross-over variants more frequently adopt more compact and constrained molecular arrangements that retain receptors in closer proximity in the plasma membrane. Thus, they can promote receptor clustering and multimerization, leading to strong agonism. In contrast, variants lacking the disulfide cross-over would sample a greater range of conformations, including those which are non-productive; therefore, they will not stabilize and cluster receptors to nucleate sufficient multimerization to surpass the signaling threshold. This mechanism conceivably also operates during the natural redox conversion of IgG2A to IgG2B subtypes in the blood (*18*), which might serve to diversify carbohydrate recognition during bacterial infection (*20*).

The impact of the *h*IgG2 isotype on agonistic antibodies has been convincingly shown for a large number of anti-*h*CD40 mAb, including a full set of clinically relevant anti-*h*CD40 mAb (*13, 14*) and three different anti-*h*CD40 antagonists (*15*). Studies extended from *h*CD40 include two additional therapeutically exciting TNFRs, namely 4-1BB and OX40, as well as *h*CD28, demonstrating equivalent activity of *h*IgG2 on an entirely different receptor family. All of these examples demonstrate the broad applicability of the *h*IgG2 isoform in driving receptor clustering to evoke agonism *(16, 37, 38)*.

With specific reference to hinge engineering, we recently provided evidence for the anti-*h*CD40 *h*IgG2 mAb 341G2 that a hinge constricted "locked B" form (C127S), but not the unrestricted "A" form (C232S/C233S), activated *h*CD40 Tg DCs *in vivo* and human DC *in vitro*, evoking antigen specific CD8 T cell expansion in an FcγR-independent manner. Significantly, this demonstrates that the *h*IgG2 hinge-mediated regulation of agonistic activity using C/S variants can be employed across a variety of *h*CD40 binding epitopes (*15*).

Therefore, although the structural analysis presented here is limited to a single antibody series, the applicability of C/S engineering is generalizable. Another potential limitation of our study was the use of $F(ab)_2$ fragments rather than full *h*IgG. This was necessitated to permit the structural analysis, and although it remains possible that full *h*IgG may operate differently, this appears unlikely as $F(ab)_2$ fragments of *h*IgG2 have been shown to convey the same activity as their parental full length *h*IgG2 (*13*). We therefore believe the data provides a conclusive molecular explanation for the agonistic *h*IgG2 hinge effect based upon conformational restriction through a disulfide switch.

Other examples of conformational regulation of antibody function have previously been described. Differential glycosylation at N297 within the Fc is known to modify conformation and affect antibody stability and efficacy (*39*). Single amino acid insertions in λ light chains influence the flex around the elbow angle connecting variable and constant F(ab) domains (*40*). Likewise, subtle modifications of F(ab) framework regions can alter the orientation of light and heavy chains with respect to each other to influence affinity (*41*). These properties have, to our knowledge, not been implemented in a therapeutic setting. The disulfide switch illustrated here adds to these engineering capabilities, providing an elegant way to modulate agonistic activity.

When developing agonistic antibodies for clinical use, hinge disulfide engineering provides a simply implemented means to influence antibody-mediated activation of immune receptors such as TNFRs (*42*), where evoking the appropriate level of activation is critical. Antibodies for treating various immune conditions or cancer are already approved, but others, especially those mediating immune activation, have been hampered by toxicity (*8, 43, 44*). Avoiding over-active responses and preventing dose-limiting toxicity will be key in these cases. Being able to control biological activity more precisely through simple hinge engineering *via* the covalent switch may thus provide a tractable means when developing mAb for clinical use.

MATERIALS AND METHODS

Study design

The laboratory study was initiated to investigate the underlying mechanism of how the *h*IgG2 isotype provides agonistic activity to immunostimulatory mAb directed to various immune receptors. We hypothesized that this property arises due to the unique disulfide patterning of the *h*IgG2 hinge. Accordingly, $F(ab)_2$ fragments of a series of anti-human CD40 ChiLob7/4 *h*IgG2 cysteine serine (C/S) exchange variants were produced and evaluated for their antibody-mediated agonism of CD40. Agonism for these variants was measured in a series of cell biology assays – all data were included, with no data or outliers excluded. Sampling and experimental replicates are indicated in each figure legend. Biological data typically involved technical triplicates with independent experiments being repeated three times. Commonly, biological data was also replicated over a series of concentrations and using different assays, with agonism evaluated through CD23 or MHC II upregulation, homotypic adhesion, cell proliferation and NFκB-GFP reporter assays. These data were used to establish a hierarchy of agonism within the C/S exchange variants for which the structural/mechanistic basis was then sought. The $F(ab)_2$ fragments were subjected to crystallization trials. Data collection included performing structure determination at an X-ray wavelength where significant anomalous scattering for sulfur atoms was observed to enable the determination of sulfur positions and disulfides. Variant conformation and flexibility were then evaluated using SAXS followed by molecular dynamics simulations and ensemble generation and fitting. Data were then evaluated in the context of relative agonism. Experiments were not blinded with experimenters aware of experimental treatments.

Antibody production and purification. We generated the anti-human (*h*) *h*CD40 ChiLob7/4 *h*IgG2 cysteine serine (C/S) exchange variants C232S+C233S, C232S, C233S, C233SκC214S, C239S and C232SκC214S. We adhere to the Kabat numbering throughout the report, even though sequential amino acid numbering was used in deposition of the structures and SAXS data. The Kabat residues C127, C232, C233, C239 and C242 equate to C136, C224, C225, C228 and C231 in the deposited models, respectively; the κ-light chain C214 is identical in both

nomenclatures. Antibodies were produced in Chinese hamster ovary (CHO) cells and purified by protein A affinity chromatography as previously described *(13)*. All antibodies were tested and determined to be endotoxin low (<10 EU/mg) using an Endosafe PTS device (Charles River Laboratories) and aggregate-free (<1%) as determined by HPLC, as described previously *(13)*. To generate $F(ab)_2$ fragments (also referred to as $F(ab')_2$ in the literature), IgG was digested with pepsin for 1-2 hours with regular observation of progress using HPLC analysis, followed by purification by size exclusion chromatography (SEC) as described previously *(13, 45)*. Additionally, pooled SEC fractions were purified on a HiTrap MabSelect SuRE protein A column (Cytiva) where necessary to remove any residual IgG and Fc. Purified $F(ab)_2$ fragments were then concentrated to ~1-10 mg/ml using VivaSpin concentrators (Vivaproducts) or Amicon Ultra Centrifugal filters (Millipore, Sigma Aldrich) with a 10,000 Da cut-off. All $F(ab)_2$ fragments were determined to be endotoxin low.

Assessment of immunostimulatory activity. Immunostimulatory activity was measured using *h*CD40 transgenic mouse B cells or primary human B cells. Mouse B cells were purified from mouse spleens using negative selection with an EasySep Mouse B Cell Isolation Kit (Stemcell Technologies). Human B cells were purified from human peripheral blood mononuclear cells (PBMCs) as described previously (*38*). PBMCs were isolated from healthy donor leukocyte cones obtained through Southampton National Blood Services with prior informed consent. The use of human blood was approved by the East of Scotland Research Ethics Service, Tayside, UK. Primary human B cells were isolated from PBMCs using magnetic negative selection kits (BioLegend Inc). B cells were subsequently incubated *in vitro* with anti-*h*CD40 mAb or $F(ab)_2$ fragments and assessed in three separate assays as before *(13)*. In brief, $1x10^5$ or $1x10^6$ B cells per well were incubated with serially diluted anti-*h*CD40 mAb or $F(ab)_2$ fragments in 96-well round-bottom plates in a total of 200 uL media. To assess B cell activation, B cells were stimulated as above and CD23 (mouse) or MHCII (human) expression evaluated after 48 hours. CD23 and MHCII are key activation markers on B cells and are increased on naïve B cells after appropriate stimulation. Upregulation was assessed by flow cytometry with phycoerythrin-labelled anti-CD23 mAb (CD23PE, Clone B3B4; BD Biosciences) or brilliant violet-labelled anti-MHCII mAb (Clone L243; BioLegend Inc). Further, homotypic adhesion of B cells was assessed as a marker of B cell activation. Cells were imaged 48 hours after the initial treatment with mAb or $F(ab)_2$ fragments, and adhesion was observed as large macroscopic cell groupings, easily visible under light microscopy. Images were captured using an Olympus CKX41 inverted microscope, running Olympus CellSens Standard software (version 2.1). To assess B cell proliferation, B cells were stimulated as above for 5 days, with 1 μCi of ^3H thymidine (PerkinElmer) added to each well for the last 18 hours of incubation. Cells were then harvested and analyzed for ^3H thymidine incorporation by scintillation counting (Topcount) *(13)*. All three assays have been extensively utilized to measure anti-*h*CD40 antibody-mediated agonism (*13-15, 21*). Immunostimulatory activity was also evaluated using Jurkat-NFκB-GFP reporter cells expressing *h*CD40, as described previously (*16*). In brief, Jurkat cells were incubated with serially diluted anti-*h*CD40 mAb or $F(ab)_2$ fragments for 24 hours at 37ºC. The degree of NFkB activation was quantified by GFP fluorescence using flow cytometry.

Assessment of antibody cell surface receptor binding. Binding of C/S variants of ChiLob 7/4 anti-*h*CD40 mAb to *h*CD40 expressed on the cell surface was assessed using Ramos B cells, which naturally express *h*CD40. Ramos cells were incubated with serially diluted anti-*h*CD40 mAb for 30 mins at 4ºC. After washing twice in FACS buffer (PBS, 1% BSA, 0.01% sodium azide) by centrifugation, remaining *h*IgG was detected by incubation with secondary PE-

conjugated polyclonal goat F(ab)$_2$ anti-*h*IgG Fcγ-specific antibody (Jackson ImmunoResearch Europe Ltd., 0.5/100) for 30 mins at 4°C, then washing twice. Cell samples were analyzed using flow cytometry.

Flow cytometry. All flow cytometry data was acquired using either a FACSCalibur or FACSCanto II (both from BD Biosciences), with data analysis performed using FCS Express software Version 3 (De Novo Software) or FlowJo (BD Biosciences).

Surface Plasmon Resonance. The binding kinetics of C/S variants of ChiLob 7/4 anti-*h*CD40 mAb and F(ab)$_2$ fragments were analyzed by surface plasmon resonance using the Biacore T200 instrument (Cytiva). Recombinant soluble *h*CD40-*h*Fc-His (R&D Systems, Inc) was immobilized onto a CM5 sensor chip (Cytiva) via amine coupling at a target level of 50 RU, according to the manufacturer's protocol. Anti-*h*CD40 mAbs and F(ab)$_2$ fragments were injected through the flow cells at 20, 4, 0.8, 0.16, and 0 nM in HBS-EP+ running buffer (Cytiva) at a flow rate of 30 µL/min at 25°C with 300 seconds for association and 300 seconds for dissociation. Regeneration of the chip was performed for 30 seconds at a flow rate of 30 µL/min using 10 mM glycine, pH 1.5. Sensorgrams were fitted with the 1:1 binding model and k_a (association rate), k_d (dissociation rate) and K_D (Equilibrium dissociation constant) were calculated using Biacore Bioevaluation software (Cytiva).

Statistics and reproducibility**.** Statistical analyses were performed using GraphPad Prism software (GraphPad). A one-way ANOVA was used, as indicated in the figure legends. Reproducibility, including technical replicates and independent biological experiments, are stated in each figure legend.

Protein Crystallization. Crystallization using sitting drop vapor diffusion in 96 well Intelliplates® (SwissSci, Switzerland) was performed with a Gryphon® crystallization robot (Art Robbins Instruments, USA). The TOPS screen *(46)* at 20°C was used as an entry screen at a protein concentration of 10 mg/ml. Initial hits were optimized by further fine-screening and the use of manual crystal micro-seeding. Crystals were needle-shaped and grew over two to six weeks, typically measuring 0.02 x 0.02 x 0.1 mm^3. Crystals of C233S, C233SκC214S, C239S and C232SκC214S grew in the trigonal space group P321, while C232S crystals were observed in the orthorhombic space group $P2_12_12_1$. The C232S+C233S variant did crystallize but diffraction could not be improved to a diffraction limit beyond ~10 Å. Seeding and cross-seeding strategies were unsuccessful for this variant.

Crystallographic data collection. Diffraction data were collected at beamlines ID30B and ID23-1 at the European Synchrotron Radiation Source ESRF (Grenoble, FR), and beamlines I03 and I23 at the Diamond Light Source (Oxford, UK). Crystals were cryo-protected in mother liquor containing 20 % v/v glycerol before cryocooling in liquid nitrogen. Data were collected at 100 K (ID30B, ID23-1, I03) or 70 K (I23). Anomalous data were collected at 1.8 Å (ESRF ID30B) or 2.755 Å (Diamond I23) incident X-ray wavelength to maximize the anomalous sulfur signal. For data collected on ID30B and ID23-1 (ESRF), a helical strategy was used to collect 3600 images at 0.1 degree oscillation per image to provide a 360 degree dataset with dose spread over the length of the needle-like crystal. For anomalous data collection at the *in-vacuo* long-wavelength beamline I23 *(28)* (Diamond Light Source) 3600 images were collected at 0.1 degree oscillation per image to give a 360 degree dataset.

Crystallographic data processing, structure determination and refinement. Data were integrated using XDS *(47)* and scaled and merged using Pointless and Aimless *(48)* for native data and with

XSCALE *(47)* for anomalous data. Data manipulation, molecular replacement and refinement were carried out with programs of the CCP4 suite *(49)*. Molecular replacement was performed with Molrep *(50)* and used PDB:1U6A as the homologous model. Model building using Coot and refinement with Refmac5 were iterated *(51, 52)*. Anomalous data were used in refinement except for C239S where anomalous data were collected at beamline I23 and refinement was carried out against higher resolution native data collected at beamline I03 (both Diamond Light Source). The final models were deposited in the Protein Data Bank with accession codes 6TKB, 6TKC, 6TKD, 6TKE and 6TKF (**Table S2**). The sulfur anomalous maps (**Fig. S1**) were obtained using ANODE that uses fully refined structures to calculate anomalous difference Fourier maps *(53)*; in this case intensities were read in using SHELXC *(54)*.

SAXS data collection. SAXS data were collected at the ESRF beamline BM29 at a wavelength of 0.99 Å at a temperature of 20 °C (Grenoble, FR) (*55*). Samples were loaded using a SEC-SAXS setup, passing through a Superdex 200 10/300 column (GE Healthcare) before entering a 1 mm quartz glass capillary to be exposed to X-rays. Scattering images were collected using a Dectris Pilatus 1M detector with a sample to detector distance of 2.9 m.

SAXS data analysis and structure fit. ScÅtter v.3.2h (*56*) and ATSAS (*57*) were used for primary data analysis, including solvent subtraction and determination of the radius of gyration (R_g) and maximal dimension (D_{max}), as well as Kratky analysis, **Fig. 3**. χ^2 fits between the crystal structures (unresolved loops and hinge regions added, see next section) and the experimental SAXS data were generated using Crysol *(58)* with constant subtraction enabled. Error-weighted residuals (Δ/σ) were calculated as I(exp)-I(model)/σ. Residuals are also displayed as lines after FFT smoothing. A model based on the C232S structure was generated for the C232S+C233S variant for which no crystal structure was available, performing *in silico* mutagenesis of C233 to S233 in PyMOL. SREFLEX (*32*) was used to perform normal mode refinement to fit coordinates to the SAXS data. Each F(ab) arm was defined as a custom domain during rigid body refinement. Hinge residues were removed to allow each F(ab) arm to move freely. The SAXS data along with the single structure and ensemble fits were deposited to the SASBDB with the accession codes SASDLF4, SASDLG4, SASDLH4, SASDLJ4, SASDLK4 and SASDLL4 (**Table S3**).

Molecular dynamics simulation (MD). Preparation of input structures for MD included model completion, removal of multiple conformations and protonation. MODELLER (v 9.19) *(59)* was used to fill in loop regions not resolved in electron density in the crystal structures. Further, hinge residues not resolved in the crystal structures but known to be present from mass spectrometry analysis were added. In regions where multiple conformations had been fitted to the electron density, the models were pruned to the major conformation. Hydrogens were added using the H++ protonation server (v 3.2) at default parameters *(60)*, where the environment pH was set to 7.0. Atomistic MD was performed using the Amber 16 and Amber 18 software packages (*61*). Protonated structures were solvated in boxes with a 25 Å buffer between protein and edge of the box, filled with pre-equilibrated water molecules using the TIP3P water model. Neutralization of the system was done through the addition of chloride ions to obviate excess positive charges, followed by addition of Na^+ and Cl^- ions to a final concentration of 150 mM NaCl. Protein atoms were represented by the Amber ff14SB force field *(62)* while ions were represented by the parameters of Joung and Cheatham *(63)*. Energy minimization was performed, using 1000 steps of a steepest descent protocol followed by 1500 steps with a conjugate gradient protocol. Heating to 300 K for 50 ps under NVT conditions (constant number of particles, volume, temperature) was followed by equilibration at 1 bar for 100 ps under NPT

conditions (constant number of particles, pressure, temperature). A Berendsen barostat set to 1 bar (*64*) with a pressure relaxation time of 2.0 ps was used to maintain pressure during system equilibration. Three independent MD runs with different random seeds for the Langevin thermostat (*65*) and starting NaCl ion positions were performed for each variant. The Langevin thermostat maintains the temperature, set to a collision frequency of 2 ps^{-1}. MD simulations used periodic boundary conditions and an 8 Å direct space cut-off for nonbonded interactions. An analytical dispersion correction was used to account for long-range van der Waals interactions. Particle Mesh Ewald summation was used for long-range electrostatics. SHAKE (*66*) was used to constrain all bonds involving hydrogen. A Monte Carlo barostat (*67*) was used throughout the 2 μs production simulations, with 100 steps between volume change attempts. All simulations used a 2 fs time step. Initial simulations were run for a total of 6 μs per variant. Further simulations were then spawned from frames of the initial simulations, starting from models showing maximal/minimal R_g values with the aim to further increase sampling. The spawned simulations were run for 200 ns under the same conditions as the initial simulations. Models were extracted from the resulting trajectories at 1 ns intervals using cpptraj *(68)*, yielding 8000 structural states for each variant.

Ensemble fitting. Ensembles of conformations were selected from the MD generated conformational pool using a genetic algorithm implemented in the program GAJOE (*35*). Ensemble selection aims to minimize the discrepancy between the computed scattering intensity of the ensemble, calculated as the average of constituent individual curves, and the experimental scattering curve. GAJOE was run 10 independent times to ensure convergence of the genetic algorithm. GAJOE was run with default parameters and the MD generated pool of models as the input; the results are shown in **Fig. 4**. A total of 100 genetic algorithm cycles were carried out per run, with each cycle comprising 1000 generations. The SAXS optimized R_g population density curve and the fit to the experimental data were plotted in R, along with representative states being displayed using PyMOL.

Definition of hinge and torsion angle. Hinge and torsion angles for $F(ab)_2$ fragments were defined between different centers of mass, as determined in PyMOL, see **Fig. S5** for reference. The angles were then determined using the angle and dihedral measurement tool in PyMOL. For the calculation of torsion angles, the center of mass for the domains was calculated as follows. Torsion angle: the variable domain included heavy chain amino acids 1 to 121 and light chain amino acids 1 to 107; the constant domain included heavy chain amino acids 125 to 220 and light chain amino acids 111 to 214. For calculation of the hinge angle, the hinge domain was included: the constant domain was calculated across the two chains of the $F(ab)_2$, encompassing heavy chain amino acids 125 to 231 and light chain amino acids 111 to 214.

Supplementary Materials

Fig. S1. Determination of agonistic activity and binding properties of ChiLob7/4 *h*IgG2 C/S variants, as $F(ab)_2$ or IgG.

Fig. S2. Conformational variation of $F(ab)_2$ variants in the two reported crystal forms.

Fig. S3. Revealing *h*IgG2 hinge disulfides and free cysteines in ChiLob7/4 *h*IgG2 C/S $F(ab)_2$ variants through anomalous scattering.

Fig. S4. Comparison of the performance of single and multiple model fitting of SAXS data derived from ChiLob7/4 *h*IgG2 C/S $F(ab)_2$ variants.

Fig. S5. Definition of $F(ab)_2$ hinge and torsion angle.

Table S1. Affinity of anti-*h*CD40 ChiLob7/4 *h*IgG2 C/S variants, as IgG and $F(ab)_2$ fragments, binding to *h*CD40.

Table S2. Crystallographic analysis of anti-*h*CD40 ChiLob7/4 *h*IgG2 C/S $F(ab)_2$ variants.

Table S3. SAXS analysis of anti-*h*CD40 ChiLob7/4 *h*IgG2 C/S $F(ab)_2$ variants.

Supplementary data file 1. Raw data excel file

References and Notes

1. L. Urquhart, Top companies and drugs by sales in 2019. *Nat Rev Drug Discov* **19**, 228 (2020).
2. A. Mullard, FDA approves 100th monoclonal antibody product. *Nat Rev Drug Discov* **20**, 491-495 (2021).
3. H. Kaplon, A. Chenoweth, S. Crescioli, J. M. Reichert, Antibodies to watch in 2022. *MAbs* **14**, 2014296 (2022).
4. L. M. Weiner, R. Surana, S. Wang, Monoclonal antibodies: versatile platforms for cancer immunotherapy. *Nat Rev Immunol* **10**, 317-327 (2010).
5. G. Vidarsson, G. Dekkers, T. Rispens, IgG subclasses and allotypes: from structure to effector functions. *Front Immunol* **5**, 520 (2014).
6. R. J. Brezski, G. Georgiou, Immunoglobulin isotype knowledge and application to Fc engineering. *Curr Opin Immunol* **40**, 62-69 (2016).
7. R. Liu, R. J. Oldham, E. Teal, S. A. Beers, M. S. Cragg, Fc-Engineering for Modulated Effector Functions-Improving Antibodies for Cancer Treatment. *Antibodies (Basel)* **9**, 64 (2020).
8. P. A. Mayes, K. W. Hance, A. Hoos, The promise and challenges of immune agonist antibody development in cancer. *Nat Rev Drug Discov* **17**, 509-527 (2018).
9. L. K. Ward-Kavanagh, W. W. Lin, J. R. Sedy, C. F. Ware, The TNF Receptor Superfamily in Co-stimulating and Co-inhibitory Responses. *Immunity* **44**, 1005-1019 (2016).
10. S. P. Schoenberger, R. E. Toes, E. I. van der Voort, R. Offringa, C. J. Melief, T-cell help for cytotoxic T lymphocytes is mediated by CD40-CD40L interactions. *Nature* **393**, 480-483 (1998).
11. R. R. French, H. T. C. Chan, A. L. Tutt, M. J. Glennie, CD40 antibody evokes a cytotoxic T-cell response that eradicates lymphoma and bypasses T-cell help. *Nature Medicine* **5**, 548-553 (1999).
12. S. A. Beers, M. J. Glennie, A. L. White, Influence of immunoglobulin isotype on therapeutic antibody function. *Blood* **127**, 1097-1101 (2016).
13. A. L. White, H. T. C. Chan, R. R. French, J. Willoughby, C. I. Mockridge, A. Roghanian, C. a. Penfold, S. G. Booth, A. Dodhy, M. E. Polak, E. a. Potter, M. R. Ardern-jones, J. S. Verbeek, P. W. M. Johnson, A. Al-shamkhani, M. S. Cragg, S. a. Beers, M. J. Glennie, Conformation of the Human Immunoglobulin G2 Hinge Imparts Superagonistic Properties to Immunostimulatory Anticancer Antibodies. *Cancer Cell* **27**, 138-148 (2015).
14. X. Yu, H. T. C. Chan, C. M. Orr, O. Dadas, S. G. Booth, L. N. Dahal, C. A. Penfold, L. O'Brien, C. I. Mockridge, R. R. French, P. Duriez, L. R. Douglas, A. R. Pearson, M. S. Cragg, I. Tews, M. J. Glennie, A. L. White, Complex Interplay between Epitope Specificity and Isotype Dictates the Biological Activity of Anti-human CD40 Antibodies. *Cancer Cell* **33**, 664-675 e664 (2018).
15. X. Yu, H. T. C. Chan, H. Fisher, C. A. Penfold, J. Kim, T. Inzhelevskaya, C. I. Mockridge, R. R. French, P. J. Duriez, L. R. Douglas, V. English, J. S. Verbeek, A. L. White, I. Tews, M. J. Glennie, M. S. Cragg, Isotype Switching Converts Anti-CD40 Antagonism to Agonism to Elicit Potent Antitumor Activity. *Cancer Cell* **37**, 850-866 e857 (2020).
16. X. J. Yu, S. James, J. H. Felce, B. Kellermayer, D. A. Johnston, H. T. C. Chan, C. A. Penfold, J. Kim, T. Inzhelevskaya, C. I. Mockridge, Y. Watanabe, M. Crispin, R. R. French, P. J. Duriez, L. R. Douglas, M. J. Glennie, M. S. Cragg, TNF receptor agonists induce distinct receptor clusters to mediate differential agonistic activity. *Commun Biol* **4**, 772 (2021).
17. T. M. Dillon, M. S. Ricci, C. Vezina, G. C. Flynn, Y. D. Liu, D. S. Rehder, M. Plant, B. Henkle, Y. Li, S. Deechongkit, B. Varnum, J. Wypych, A. Balland, P. V. Bondarenko, Structural and functional characterization of disulfide isoforms of the human IgG2 subclass. *J Biol Chem* **283**, 16206-16215 (2008).

18. J. Wypych, M. Li, A. Guo, Z. Zhang, T. Martinez, M. J. Allen, S. Fodor, D. N. Kelner, G. C. Flynn, Y. D. Liu, P. V. Bondarenko, M. S. Ricci, T. M. Dillon, A. Balland, Human IgG2 antibodies display disulfide-mediated structural isoforms. *J Biol Chem* **283**, 16194-16205 (2008).
19. B. Zhang, A. G. Harder, H. M. Connelly, L. L. Maheu, S. L. Cockrill, Determination of Fab-hinge disulfide connectivity in structural isoforms of a recombinant human immunoglobulin G2 antibody. *Anal Chem* **82**, 1090-1099 (2010).
20. R. Jefferis, D. S. Kumararatne, Selective IgG subclass deficiency: quantification and clinical relevance. *Clin Exp Immunol* **81**, 357-367 (1990).
21. A. L. White, L. Dou, H. T. Chan, V. L. Field, C. I. Mockridge, K. Moss, E. L. Williams, S. G. Booth, R. R. French, E. A. Potter, C. Butts, A. Al-Shamkhani, M. S. Cragg, J. S. Verbeek, P. W. Johnson, M. J. Glennie, S. A. Beers, Fcgamma receptor dependency of agonistic CD40 antibody in lymphoma therapy can be overcome through antibody multimerization. *J Immunol* **193**, 1828-1835 (2014).
22. S. L. Buchan, L. Dou, M. Remer, S. G. Booth, S. N. Dunn, C. Lai, M. Semmrich, I. Teige, L. Martensson, C. A. Penfold, H. T. C. Chan, J. E. Willoughby, C. I. Mockridge, L. N. Dahal, K. L. S. Cleary, S. James, A. Rogel, P. Kannisto, M. Jernetz, E. L. Williams, E. Healy, J. S. Verbeek, P. W. M. Johnson, B. Frendeus, M. S. Cragg, M. J. Glennie, J. C. Gray, A. Al-Shamkhani, S. A. Beers, Antibodies to Costimulatory Receptor 4-1BB Enhance Anti-tumor Immunity via T Regulatory Cell Depletion and Promotion of CD8 T Cell Effector Function. *Immunity* **49**, 958-970 e957 (2018).
23. J. Griffiths, K. Hussain, H. L. Smith, T. Sanders, K. L. Cox, M. Semmrich, L. Martensson, J. Kim, T. Inzhelevskaya, C. A. Penfold, A. L. Tutt, C. I. Mockridge, H. C. Chan, V. English, R. F. French, I. Teige, A. Al-Shamkhani, M. J. Glennie, B. L. Frendeus, J. E. Willoughby, M. S. Cragg, Domain binding and isotype dictate the activity of anti-human OX40 antibodies. *J Immunother Cancer* **8**, (2020).
24. G. G. Klaus, M. Holman, J. Hasbold, Properties of mouse CD40: the role of homotypic adhesion in the activation of B cells via CD40. *Eur J Immunol* **24**, 2714-2719 (1994).
25. A. L. White, H. T. Chan, A. Roghanian, R. R. French, C. I. Mockridge, A. L. Tutt, S. V. Dixon, D. Ajona, J. S. Verbeek, A. Al-Shamkhani, M. S. Cragg, S. A. Beers, M. J. Glennie, Interaction with FcgammaRIIB is critical for the agonistic activity of anti-CD40 monoclonal antibody. *J Immunol* **187**, 1754-1763 (2011).
26. J. Nomura, S. Inui, T. Yamasaki, S. Kataoka, K. Maeda, K. Nakanishi, N. Sakaguchi, Anti-CD40 monoclonal antibody induces the proliferation of murine B cells as a B-cell mitogen through a distinct pathway from receptors for antigens or lipopolysaccharide. *Immunol Lett* **45**, 195-203 (1995).
27. L. J. Harris, E. Skaletsky, A. McPherson, Crystallographic structure of an intact IgG1 monoclonal antibody. *J Mol Biol* **275**, 861-872 (1998).
28. A. Wagner, R. Duman, K. Henderson, V. Mykhaylyk, In-vacuum long-wavelength macromolecular crystallography. *Acta Crystallogr D Struct Biol* **72**, 430-439 (2016).
29. E. Krissinel, K. Henrick, Inference of macromolecular assemblies from crystalline state. *J Mol Biol* **372**, 774-797 (2007).
30. C. D. Putnam, M. Hammel, G. L. Hura, J. A. Tainer, X-ray solution scattering (SAXS) combined with crystallography and computation: defining accurate macromolecular structures, conformations and assemblies in solution. *Q Rev Biophys* **40**, 191-285 (2007).
31. R. P. Rambo, J. A. Tainer, Characterizing Flexible and Intrinsically Unstructured Biological Macromolecules by SAS Using the Porod-Debye Law. *Biopolymers* **95**, 559-571 (2011).
32. A. Panjkovich, D. I. Svergun, Deciphering conformational transitions of proteins by small angle X-ray scattering and normal mode analysis. *Phys Chem Chem Phys* **18**, 5707-5719 (2016).
33. S. P. Meisburger, W. C. Thomas, M. B. Watkins, N. Ando, X-ray Scattering Studies of Protein Structural Dynamics. *Chemical Reviews* **117**, 7615-7672 (2017).
34. M. Bonomi, G. T. Heller, C. Camilloni, M. Vendruscolo, Principles of protein structural ensemble determination. *Curr Opin Struct Biol* **42**, 106-116 (2017).
35. P. Bernado, E. Mylonas, M. V. Petoukhov, M. Blackledge, D. I. Svergun, Structural characterization of flexible proteins using small-angle X-ray scattering. *J Am Chem Soc* **129**, 5656-5664 (2007).
36. G. Tria, H. D. Mertens, M. Kachala, D. I. Svergun, Advanced ensemble modelling of flexible macromolecules using X-ray solution scattering. *IUCrJ* **2**, 207-217 (2015).
37. H. Wajant, Principles of antibody-mediated TNF receptor activation. *Cell Death Differ* **22**, 1727-1741 (2015).
38. J. D. Graves, J. J. Kordich, T. H. Huang, J. Piasecki, T. L. Bush, T. Sullivan, I. N. Foltz, W. Chang, H. Douangpanya, T. Dang, J. W. O'Neill, R. Mallari, X. Zhao, D. G. Branstetter, J. M. Rossi, A. M. Long, X.

Huang, P. M. Holland, Apo2L/TRAIL and the death receptor 5 agonist antibody AMG 655 cooperate to promote receptor clustering and antitumor activity. *Cancer Cell* **26**, 177-189 (2014).
39. P. Zhang, S. Woen, T. Wang, B. Liau, S. Zhao, C. Chen, Y. Yang, Z. Song, M. R. Wormald, C. Yu, P. M. Rudd, Challenges of glycosylation analysis and control: an integrated approach to producing optimal and consistent therapeutic drugs. *Drug Discov Today* **21**, 740-765 (2016).
40. R. L. Stanfield, A. Zemla, I. A. Wilson, B. Rupp, Antibody elbow angles are influenced by their light chain class. *J Mol Biol* **357**, 1566-1574 (2006).
41. J. Dunbar, A. Fuchs, J. Shi, C. M. Deane, ABangle: characterising the VH-VL orientation in antibodies. *Protein Eng Des Sel* **26**, 611-620 (2013).
42. E. S. Vanamee, D. L. Faustman, Structural principles of tumor necrosis factor superfamily signaling. *Sci Signal* **11**, eaao4910 (2018).
43. T. Bartkowiak, A. R. Jaiswal, C. R. Ager, R. Chin, C. H. Chen, P. Budhani, M. Ai, M. J. Reilley, M. M. Sebastian, D. S. Hong, M. A. Curran, Activation of 4-1BB on Liver Myeloid Cells Triggers Hepatitis via an Interleukin-27-Dependent Pathway. *Clin Cancer Res* **24**, 1138-1151 (2018).
44. N. H. Segal, T. F. Logan, F. S. Hodi, D. McDermott, I. Melero, O. Hamid, H. Schmidt, C. Robert, V. Chiarion-Sileni, P. A. Ascierto, M. Maio, W. J. Urba, T. C. Gangadhar, S. Suryawanshi, J. Neely, M. Jure-Kunkel, S. Krishnan, H. Kohrt, M. Sznol, R. Levy, Results from an Integrated Safety Analysis of Urelumab, an Agonist Anti-CD137 Monoclonal Antibody. *Clin Cancer Res* **23**, 1929-1936 (2017).
45. C. Milstein, B. Frangione, Disulphide bridges of the heavy chain of human immunoglobulin G2. *Biochem J* **121**, 217-225 (1971).
46. A. M. Bulek, F. Madura, A. Fuller, C. J. Holland, A. J. A. Schauenburg, A. K. Sewell, P. J. Rizkallah, D. K. Cole, TCR/pMHC Optimized Protein crystallization Screen. *J Immunol Methods* **382**, 203-210 (2012).
47. W. Kabsch, Xds. *Acta Crystallogr D* **66**, 125-132 (2010).
48. P. R. Evans, An introduction to data reduction: Space-group determination, scaling and intensity statistics. *Acta Crystallogr D* **67**, 282-292 (2011).
49. M. D. Winn, C. C. Ballard, K. D. Cowtan, E. J. Dodson, P. Emsley, P. R. Evans, R. M. Keegan, E. B. Krissinel, A. G. W. Leslie, A. McCoy, S. J. McNicholas, G. N. Murshudov, N. S. Pannu, E. A. Potterton, H. R. Powell, R. J. Read, A. Vagin, K. S. Wilson, Overview of the CCP4 suite and current developments. *Acta Crystallogr D* **67**, 235-242 (2011).
50. A. A. Vagin, A. Teplyakov, MOLREP: an Automated Program for Molecular Replacement. *J Appl Crystallogr* **30**, 1022-1025 (1997).
51. P. Emsley, B. Lohkamp, W. G. Scott, K. Cowtan, Features and development of Coot. *Acta Crystallogr D* **66**, 486-501 (2010).
52. G. N. Murshudov, A. A. Vagin, E. J. Dodson, Refinement of macromolecular structures by the maximum-likelihood method. *Acta Cryst D* **53**, 240-255 (1997).
53. A. Thorn, G. M. Sheldrick, ANODE: anomalous and heavy-atom density calculation. *J Appl Crystallogr* **44**, 1285-1287 (2011).
54. G. M. Sheldrick, Experimental phasing with SHELXC/D/E: combining chain tracing with density modification. *Acta Crystallogr D* **66**, 479-485 (2010).
55. P. Pernot, A. Round, R. Barrett, A. De Maria Antolinos, A. Gobbo, E. Gordon, J. Huet, J. Kieffer, M. Lentini, M. Mattenet, Upgraded ESRF BM29 beamline for SAXS on macromolecules in solution. *J Synchrotron Rad* **20**, 660-664 (2013).
56. N. P. Cowieson, C. J. C. Edwards-Gayle, K. Inoue, N. S. Khunti, J. Doutch, E. Williams, S. Daniels, G. Preece, N. A. Krumpa, J. P. Sutter, M. D. Tully, N. J. Terrill, R. P. Rambo, Beamline B21: high-throughput small-angle X-ray scattering at Diamond Light Source. *J Synchrotron Radiat* **27**, 1438-1446 (2020).
57. M. V. Petoukhov, D. Franke, A. V. Shkumatov, G. Tria, A. G. Kikhney, M. Gajda, C. Gorba, H. D. Mertens, P. V. Konarev, D. I. Svergun, New developments in the ATSAS program package for small-angle scattering data analysis. *J Appl Crystallogr* **45**, 342-350 (2012).
58. D. Svergun, C. Barberato, M. H. Koch, CRYSOL - A program to evaluate X-ray solution scattering of biological macromolecules from atomic coordinates. *J Appl Crystallogr* **28**, 768-773 (1995).
59. B. Webb, A. Sali, Comparative protein structure modeling using MODELLER. *Curr Prot Bioinform* **54**, 5.6, 1-37 (2016).
60. R. Anandakrishnan, B. Aguilar, A. V. Onufriev, H++ 3.0: automating p K prediction and the preparation of biomolecular structures for atomistic molecular modeling and simulations. *Nucl Acid Res* **40**, W537-W541 (2012).

61. D. A. Case, T. E. Cheatham, T. Darden, H. Gohlke, R. Luo, K. M. Merz, A. Onufriev, C. Simmerling, B. Wang, R. J. Woods, The Amber biomolecular simulation programs. *J Comp Chem* **26**, 1668-1688 (2005).
62. J. A. Maier, C. Martinez, K. Kasavajhala, L. Wickstrom, K. E. Hauser, C. Simmerling, ff14SB: improving the accuracy of protein side chain and backbone parameters from ff99SB. *J Chem Theorc Comp* **11**, 3696-3713 (2015).
63. I. S. Joung, T. E. Cheatham III, Determination of alkali and halide monovalent ion parameters for use in explicitly solvated biomolecular simulations. *J Phys Chem B* **112**, 9020-9041 (2008).
64. H. J. C. Berendsen, J. P. M. Postma, W. F. van Gunsteren, A. DiNola, J. R. Haak, Molecular dynamics with coupling to an external bath. *J Chem Phys* **81**, 3684-3690 (1984).
65. J. A. Izaguirre, D. P. Catarello, J. M. Wozniak, R. D. Skeel, Langevin stabilization of molecular dynamics. *J Chem Phys* **114**, 2090-2098 (2001).
66. J. P. Ryckaert, G. Ciccotti, H. J. C. Berendsen, Numerical integration of the cartesian equations of motion of a system with constraints: molecular dynamics of n-alkanes. *J Comp Phys* **23**, 327-341 (1977).
67. S. Duane, A. D. Kennedy, B. J. Pendleton, D. Roweth, Hybrid Monte Carlo. *Phys Lett B* **195**, 216-222 (1987).
68. D. Roe, PTRAJ and CPPTRAJ: software for processing and analysis of molecular dynamics trajectory data. *J Chem Theor Comp* **9**, 3084-3095 (2013).

Acknowledgments: We thank staff at the European Synchrotron Radiation Facility and Diamond Light Source for excellent support with data collection. We would like to thank Mark Tully at ESRF/EMBL for special help with SAXS data collection and data analysis, using beamline ESRF/B29. We thank Chris Holes at the Macromolecular Crystallisation Facility, Biological Sciences. The authors acknowledge the use of the IRIDIS and JADE High Performance Computing Facilities in the completion of this work.

Funding: Funding was provided by CRUK grants C1477/A10834, C1477/A20537, C34999/A18087 and C328/A25139 as well as EU FP7 grant 602262-2. IRIDIS is funded by the University of Southampton. Time on the JADE High Performance Computing Facilities was awarded through the HECBioSim consortium (EPSRC grant EP/R029407/1). CMO was funded by a studentship from Cancer Sciences, University of Southampton, University of Hamburg alongside a Vice-Chancellor's award to ALW. CMO and ARP were supported by the Cluster of Excellence 'The Hamburg Centre for Ultrafast Imaging' of the Deutsche Forschungsgemeinschaft (DFG EXC1074). HF was funded by a studentship from CRUK and the School of Biological Sciences, University of Southampton. XY is funded by a Faculty of Medicine Careertrack award and the Centre for Cancer Immunology TalentFund. IE is supported by a studentship from CRUK relating to programme DRCDDRPGM-Apr2020\100005. YG was supported by a studentship from the International Max Planck Research School for Ultrafast Imaging and Structural Dynamics (UFAST). ARP is supported by the Cluster of Excellence 'CUI: Advanced Imaging of Matter' (DFG EXC 2056).

Author contributions: Conceptualization – MJG, ALW, JWE, ARP, MSC, IT; Investigation – CMO, HF, XY, PJD, SGB, IE, TI, IM, ALW; Resources - XY, SGB, TI, CHTC, MJG, ALW, MSC, IT; Methodology – HF, AW, JWE, ARP; Software, YG; Formal Analysis, Data Curation and Validation – CMO, HF, YG, JWE, MSC, IT; Visualization – CMO, HF; Supervision – AW, MJG, JWE, ARP, MSC, IT; Writing – Review and Editing – CMO, HF, JWE, ARP, MSC, IT; Writing – Original Draft – ARP, MSC, IT; Funding Acquisition – AW, MJG, JWE, ARP, MSC, IT.

Competing interests: MSC acts as a retained consultant for BioInvent International, consults for several biotech companies and receives institutional payments and royalties from antibody licenses. He has received research funding from BioInvent, GSK, iTeos, UCB and Roche. MJG

acts as a consultant to several biotech companies and receives institutional payments and royalties from antibody licenses. This work is related to patent Family WO 2015/145360 protecting antibodies containing modified *h*IgG2 domains which elicit agonistic or antagonistic properties. JWE receives funding from: GSK, AZ, Syngenta, Astex, Sygnature, UCB and dstl. All other authors declare that they have no competing interests.

Data and materials availability: Crystallographic data has been deposited in the Protein Data Bank with accession codes 6TKB, 6TKC, 6TKD, 6TKE and 6TKF (**Table S2**). All data needed to evaluate the conclusions in the paper are present in the paper or the Supplementary Materials. Request for materials will be subject to a standard MTA with the University of Southampton.

737 **Figures**:

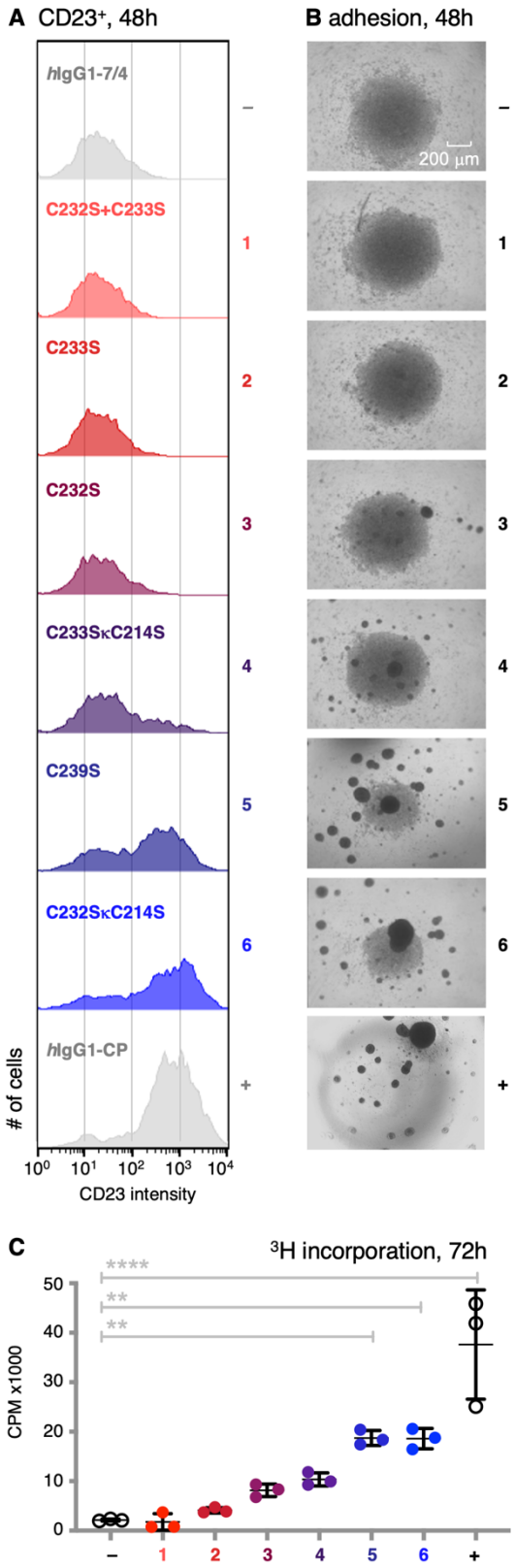

738

Fig. 1. Determination of agonistic activity of ChiLob7/4 *h*IgG2 F(ab)$_2$ variants. (A) Flow cytometry plots of *h*CD40 transgenic B cells 48h after addition of anti-*h*CD40 mAb. Fluorescence intensity (arbitrary units) arising from PE-labelled anti-CD23 mAb plotted against cell count. Plots are representative from n=3. Scale bar: 200 µm. **(B)** Homotypic adhesion of *h*CD40 transgenic B cells measured 48h after addition of anti-*h*CD40 mAb. Higher levels of cell-cell clustering (densely packed dark regions) indicate greater B cell activation. Images are a representative from n=3. **(C)** *h*CD40 transgenic B cell proliferation assessed by determining ^{3}H-thymidine incorporation 72h after addition of anti-*h*CD40 mAb; CPM = counts per minute; means ± SD; n=3; ** $p < 0.01$, **** $p < 0.0001$ using a one way ANOVA. mAb variants are numbered from 1-6 in all panels. The color scheme in A and C indicates increasing agonist activity from red to blue, with controls in grey; negative control: ChiLob7/4 *h*IgG1 (*h*IgG1-7/4); positive control: super-agonist CP870,893 *h*IgG1 (*h*IgG1-CP) (*13, 14*).

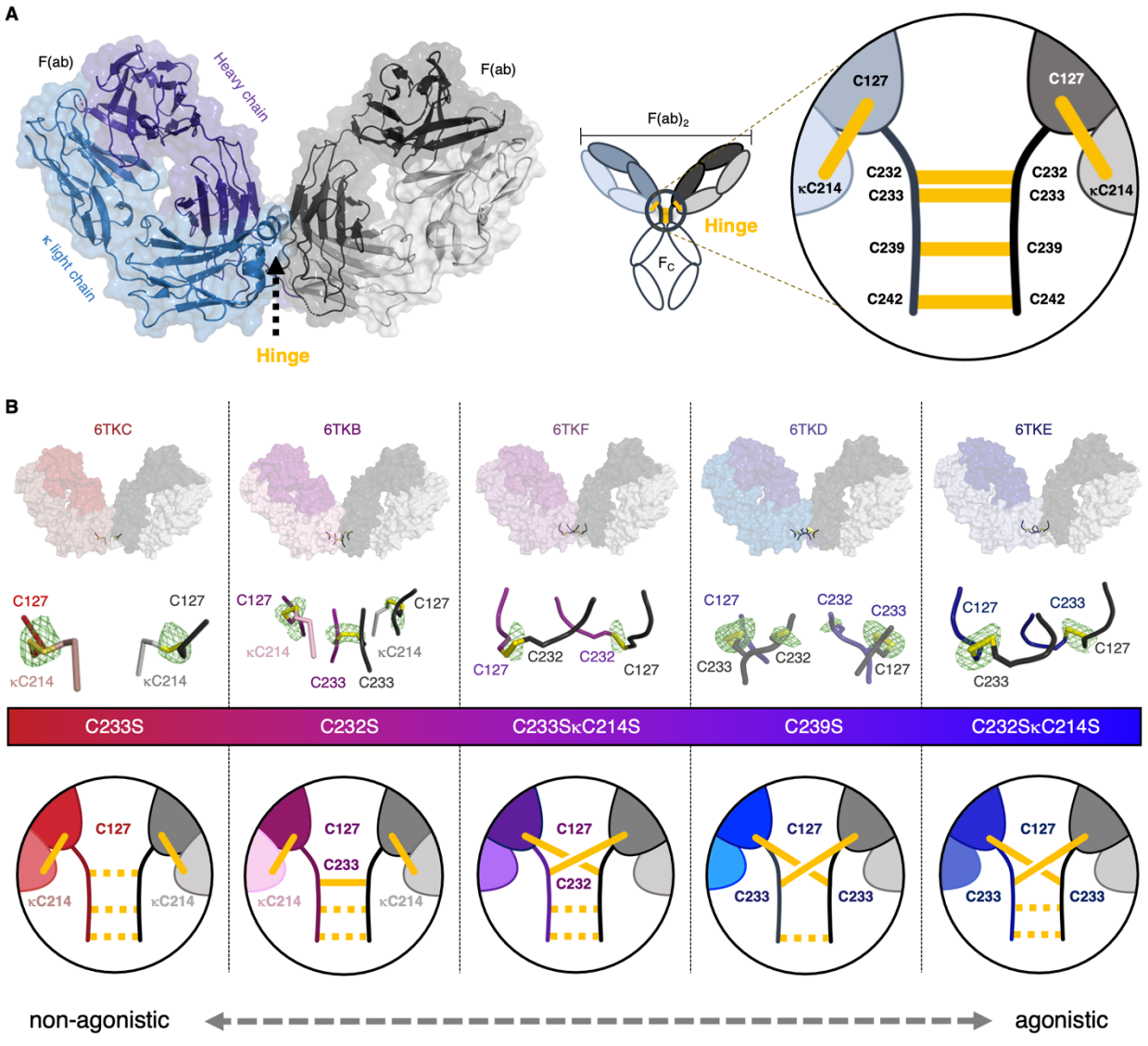

Fig. 2. Crystallographic analysis revealing the topology of hinge disulfides in ChiLob7/4 *h*IgG2 F(ab)$_2$ variants. (A) Left, the F(ab)$_2$ structure is formed by two heavy/light chain pairs, with the hinge region located between the two arms, shown as cartoon and molecular surface for 6KTD. Right, scheme for the full *h*IgG2, where the expanded hinge highlights the predicted 'paired ladder' topology of the native *h*IgG2 A-isoform; the Fc region, shown by open ovals, is not represented. **(B)** Surface representation of structures determined, with differences in the hinge expanded in stick representation (backbone colors matched to chain, disulfide bonds in yellow); the observed electron density is shown as green mesh (anomalous difference Fourier map, contoured at 4.5σ). Representations at the bottom show experimentally determined disulfides as solid lines (proposed disulfides, not resolved in electron density, are dashed). Increasing agonist activity from red to blue.

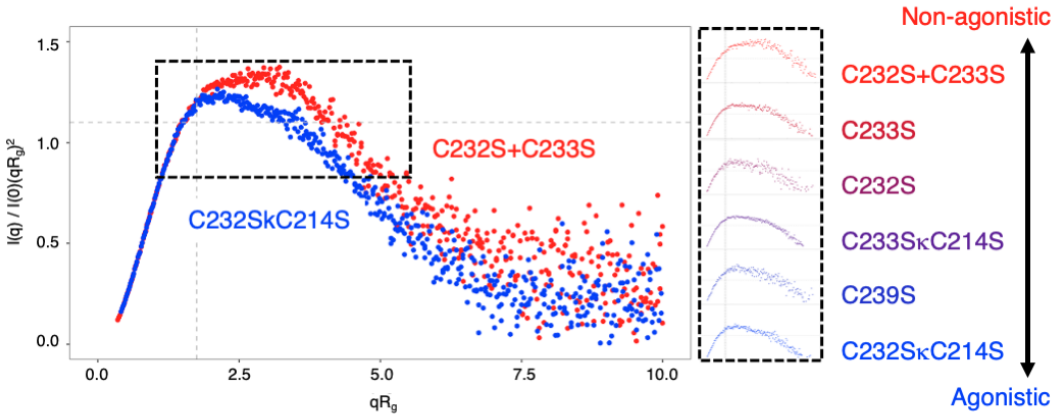

Fig. 3. Small-angle X-ray scattering (SAXS) for the six ChiLob7/4 *h*IgG2 F(ab)$_2$ C/S variants, Kratky plot analysis. The deviation from a Gaussian distribution in the dimensionless Kratky plot with a peak at the Guinier-Kratky point (grey crosshairs) indicates a departure from a rigid, globular particle for all 6 variants. The displacement of the peak up and to the right indicates varying degrees of flexibility and elongation of the samples. The extent of this deviation corresponds with activity (black dashed box), with the less agonistic, A-like variants (red) indicating greater flexibility that the more agonistic, B-like variants (blue). Increasing agonist activity from red to blue.

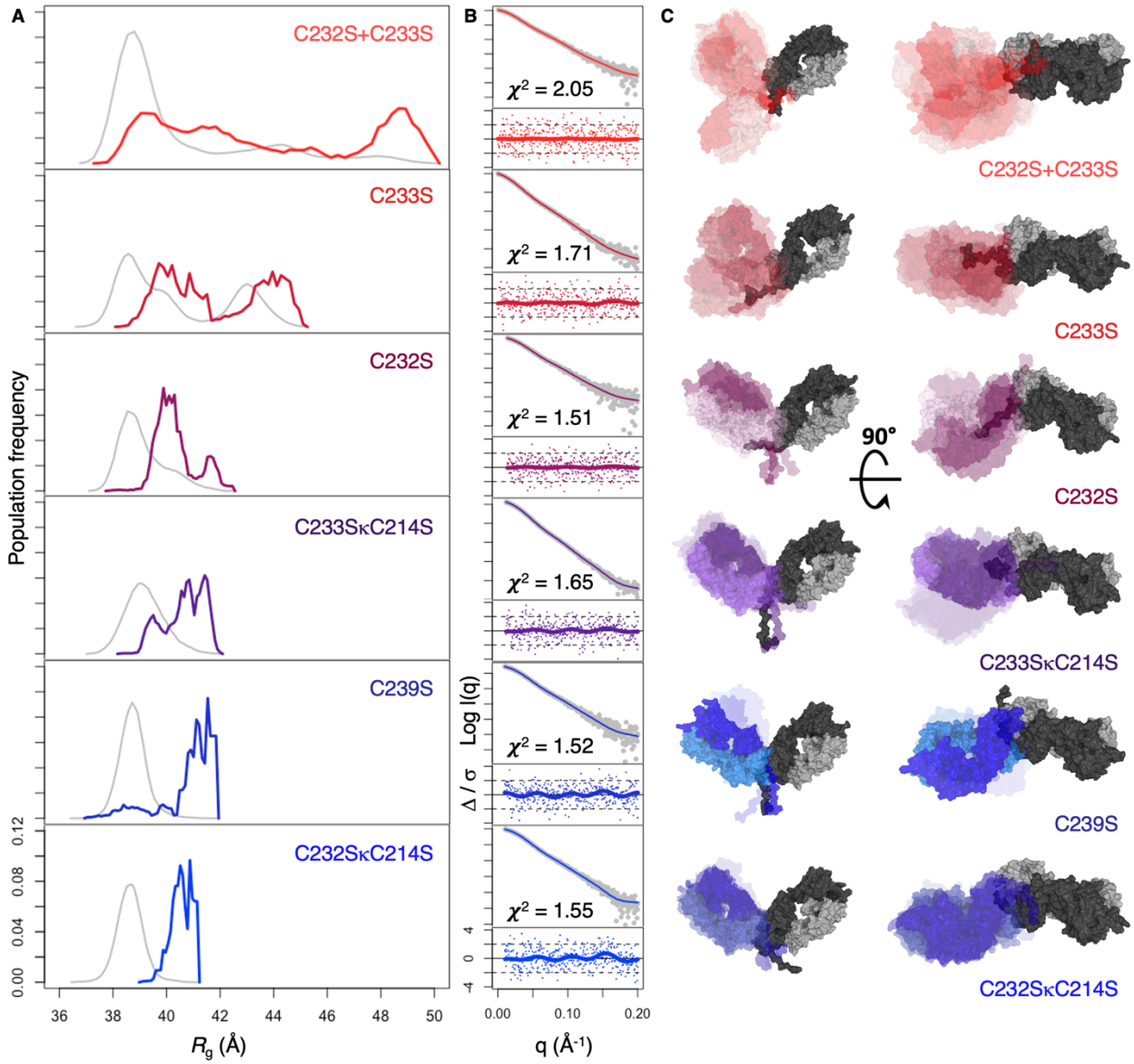

Fig. 4. Conformational states of ChiLob7/4 *h*IgG2 F(ab)$_2$ fragments revealed by combined SAXS/MD analysis. (A) Distribution of structures for all variants plotted against their calculated R_g values, where the MD pool is shown in grey and the SAXS reweighted ensemble pool selected by GAJOE (*35*) is shown in color; increasing agonist activity from red to blue as in **Fig. 1**. **(B)** Agreement of the calculated scattering curve from the reweighted ensemble with experimental SAXS data (grey dots) as indicated by χ^2 fit; the error-weighted residual plot below. **(C)** Representative conformational states are shown with one of the F(ab) arms aligned (grey) and the second F(ab) arm colored; color saturation indicates contribution to the ensemble.

Supplementary Materials for

Hinge disulfides in human IgG2 CD40 antibodies modulate receptor signaling by regulation of conformation and flexibility

Authors: Christian M Orr, [1,2,3,4,†] Hayden Fisher, [1,2,†] Xiaojie Yu, [2] Claude HT Chan, [2] Yunyun Gao, [3,5,6] Patrick J. Duriez, [2,7] Steven G. Booth, [2] Isabel Elliott, [1,2,8] Tatyana Inzhelevskaya, [2] Ian Mockridge, [2] Christine A. Penfold, [2] Armin Wagner, [4] Martin J. Glennie, [2] Ann L. White, [2,9] Jonathan W. Essex, [8,10,‡] Arwen R. Pearson, [3,5,‡] Mark S. Cragg, [2,10,‡] Ivo Tews, [1,10, ‡,*]

Affiliations:

[1]University of Southampton, Biological Sciences; Southampton SO17 1BJ, UK.

[2]University of Southampton, Centre for Cancer Immunology; Southampton, SO16 6YD, UK.

[3]Hamburg Centre for Ultrafast Imaging CFEL; Hamburg 22761, Germany.

[4]Diamond Light Source; Didcot, OX11 0FA, UK.

[5]Institute for Nanostructure and Solid State Physics; Hamburg 22761, Germany.

[6]Max Planck Institute for the Structure and Dynamics of Matter; Hamburg 22761, Germany.

[7]University of Southampton, CRUK Protein Core Facility; Southampton, SO16 6YD, UK.

[8]University of Southampton, School of Chemistry; Southampton SO17 1BJ, UK.

[9]UCB Pharma; Slough, SL1 3WE, UK.

[10]University of Southampton, Institute for Life Sciences; Southampton SO17 1BJ, UK.

*Corresponding author. Email: ivo.tews@soton.ac.uk

†These authors contributed equally

‡Senior authors

This PDF file includes:

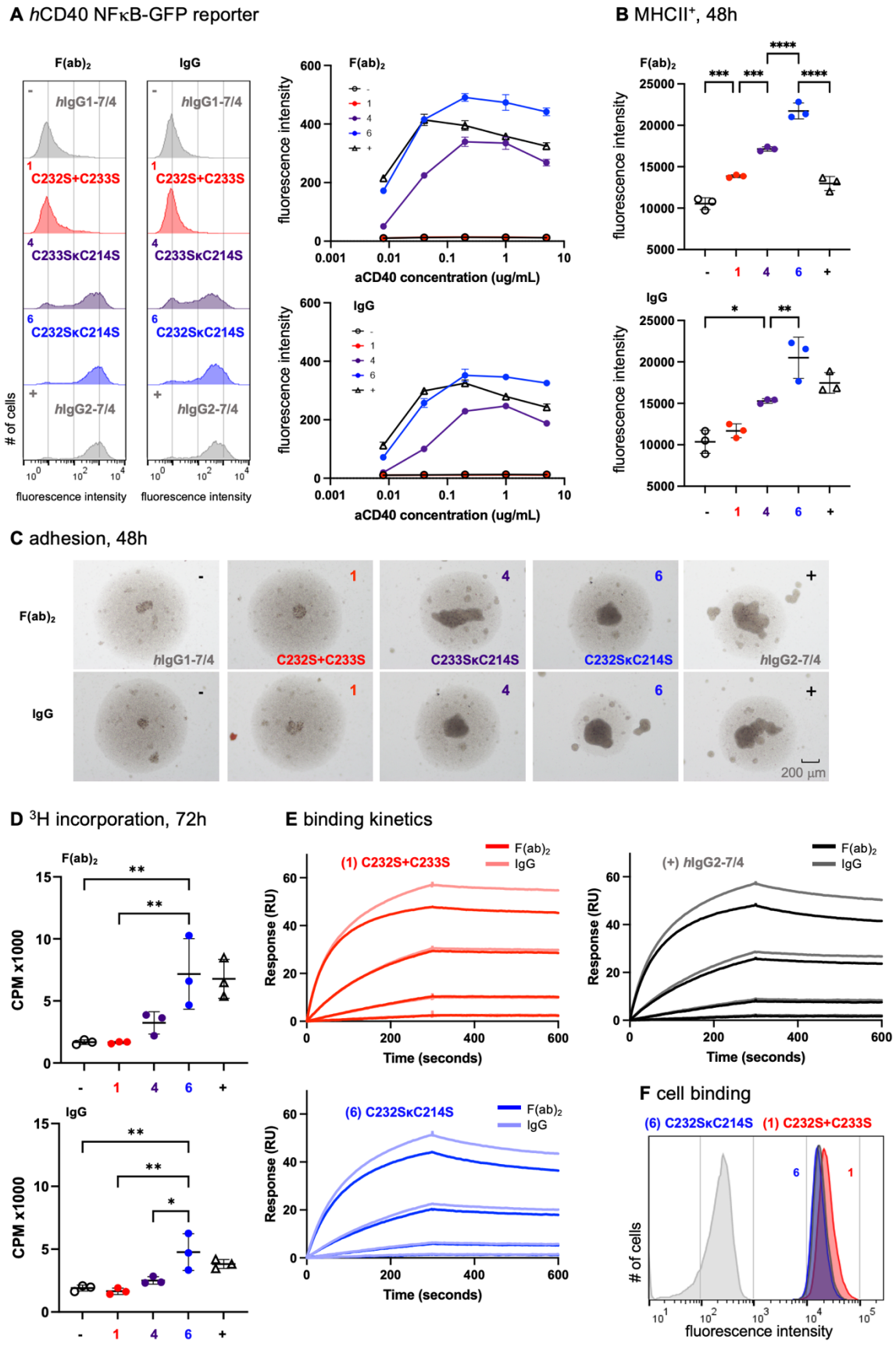
A hCD40 NFκB-GFP reporter
F(ab)2
IgG
hIgG1-7/4
C232S+C233S
C233SκC214S
C232SκC214S
hIgG2-7/4
# of cells
fluorescence intensity
aCD40 concentration (ug/mL)
B MHCII+, 48h
C adhesion, 48h
200 µm
D 3H incorporation, 72h
CPM x1000
E binding kinetics
(1) C232S+C233S
(+) hIgG2-7/4
(6) C232SκC214S
Response (RU)
Time (seconds)
F cell binding

Figure S1. Determination of agonistic activity of ChiLob7/4 *h*IgG2 variants, as F(ab)$_2$ or IgG on human cells. (A) Jurkat-NFκB-GFP reporter cells expressing *h*CD40 were incubated for 24h at 37°C with serially diluted anti-*h*CD40 mAb C/S variants as indicated. NFκB activation was quantified by determination of GFP expression levels as assessed by flow cytometry. Panels on the left show representative flow cytometry histograms. Panels on the right show dose response curves of geometric mean fluorescence intensity for F(ab)$_2$ (upper panel) or IgG (lower panel). Means ± SD, n = 3. **(B)** Primary human B cell activation was determined by MHCII upregulation. B cells were isolated from human PBMCs and stimulated with 1 µg/mL anti-*h*CD40 mAb C/S variants for 48h as indicated, shown for F(ab)$_2$ (upper panel) or IgG (lower panel). B cells were stained for anti-MHCII and evaluated by flow cytometry. Plots show median fluorescence intensity. Means ± SD, n=3. One-way ANOVA; * $p < 0.1$, ** $p < 0.01$, *** $p < 0.001$, **** $p < 0.0001$. **(C)** Homotypic adhesion of primary human B cells was determined 48h after addition of 1 µg/mL of anti-*h*CD40 mAb C/S variants for F(ab)$_2$ (upper panels) or IgG (lower panels). Images are a representative from n=3. Scale bar: 200 µm. **(D)** Primary human B cell proliferation was assessed by determining ^{3}H-thymidine incorporation 72h after addition of 1 µg/mL anti-*h*CD40 mAb C/S variants for F(ab)$_2$ (left panel) or IgG (right panel). Means ± SD, n=3. CPM = counts per minute. One-way ANOVA; * $p < 0.1$, ** $p < 0.01$. **(E)** Binding kinetics as determined by SPR using a Biacore T200 instrument. Recombinant *h*CD40-hFc-His was immobilized onto a CM5 chip *via* amine coupling. Indicated anti-*h*CD40 mAb C/S variants were injected at 20, 4, 0.8, 0.16 and 0 nM concentration. Both association and dissociation phases lasted 300 secs each. Sensorgrams were fitted using 1:1 binding model: F(ab)$_2$ (dark lines) or IgG (light lines); RU correlates with the amount of injected mAb in each plot. Data are representative of 3 independent experiments. k_a (association rate), k_d (dissociation rate) and K_D (Equilibrium dissociation constant) were calculated using the Biacore Bioevaluation software (Cytiva) and reported in **Table S1**. **(F)** Ramos cells were incubated with 20 nM anti-*h*CD40 mAb for 30 mins at 4°C. Binding was detected with a secondary PE-conjugated polyclonal goat F(ab)$_2$ anti-*h*Fc, using flow cytometry. Panels show representative flow cytometry histogram overlays (light gray, isotype control; dark gray, ChiLob7/4 *h*IgG2, colored for anti-*h*CD40 mAb C/S variants, compare Fig. 1).

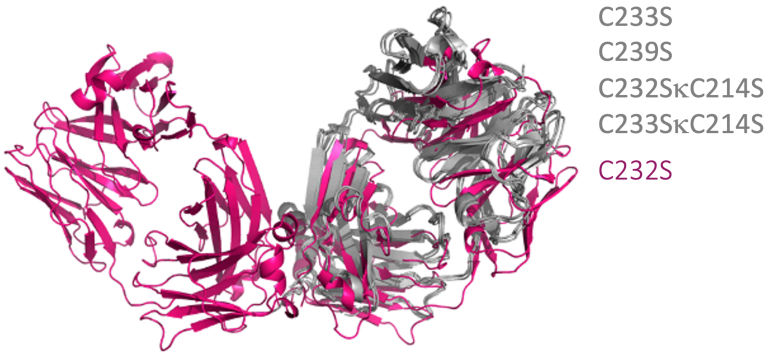

Figure S2. Conformational variation of F(ab)$_2$ variants in the two reported crystal forms. The five crystal structures determined here reveal similar overall conformation for the F(ab)$_2$ fragment in two crystal forms. In the orthorhombic unit cell seen for the C232S variant the F(ab)$_2$ fragment is a little more extended compared to the conformation observed in the trigonal cell seen for C233S, C233SκC214S, C239S, C232SκC214S variants where the F(ab) arms more closely together, leading to more compact structures.

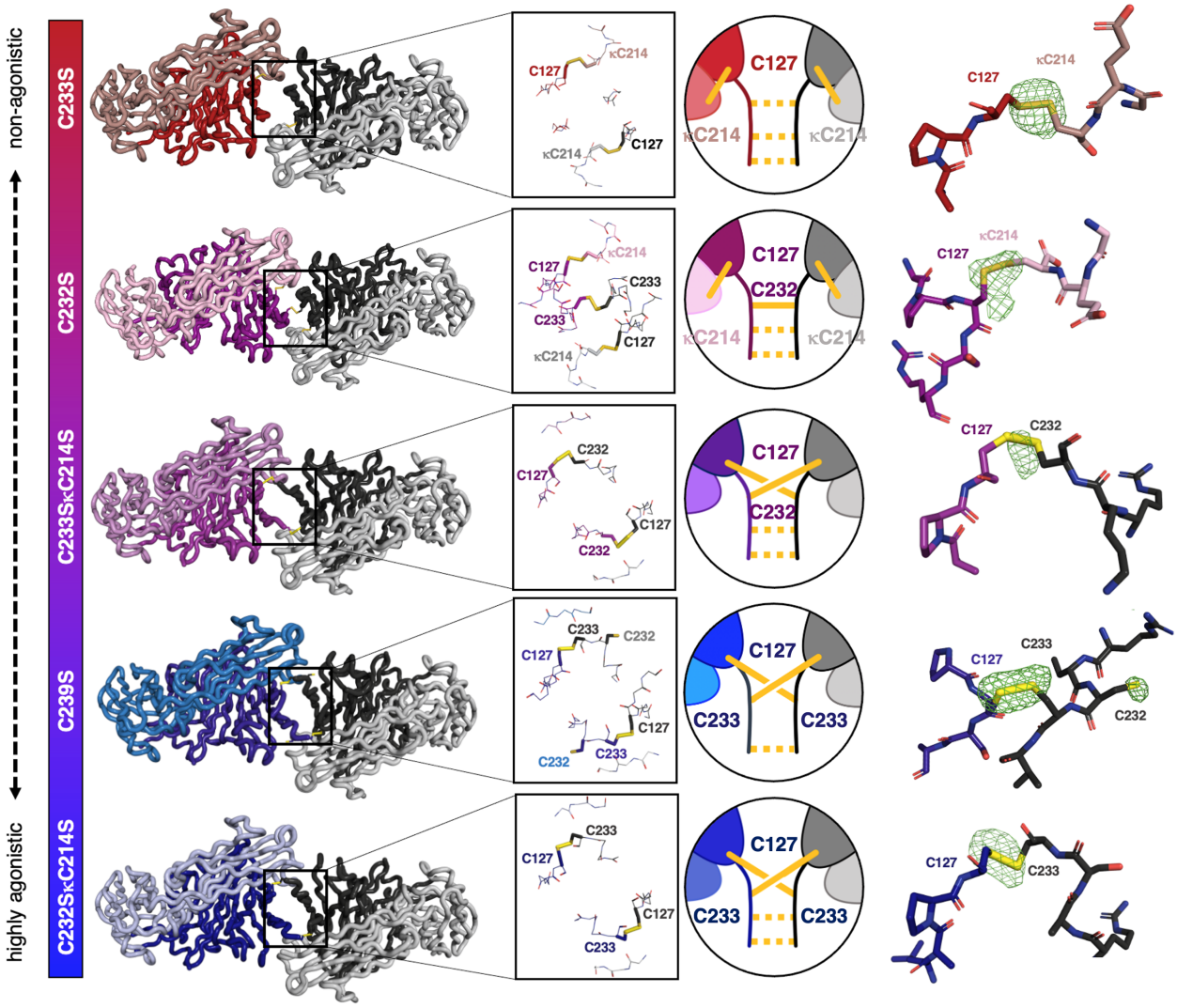

Figure S3. Revealing *h*IgG2 hinge disulfides and free cysteines in ChiLob7/4 *h*IgG2 C/S F(ab)$_2$ variants through anomalous scattering. Five crystallographic structures were determined, see also **Table S2**, shown here from low (bottom) to high (top) agonistic activity. While the overall conformation of the F(ab)$_2$ is similar in the crystal (left), differences exist with respect to disulfide bonding pattern (middle). Experimental anomalous density at 4.5 σ is shown against a stick model of the hinge region (right) to indicate the position of sulfur atoms. This experiment allowed determination of the presence of disulfides.

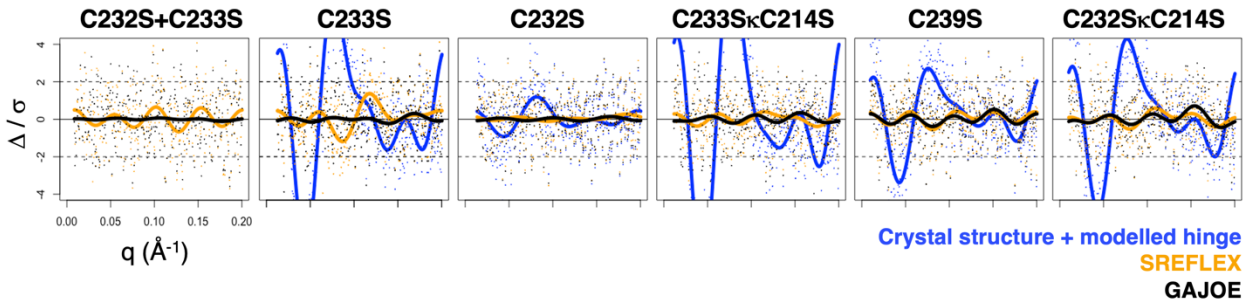

Figure S4. Comparison of the performance of single and multiple model fitting of SAXS data derived from ChiLob7/4 *h*IgG2 C/S F(ab)$_2$ variants. Compared here are the error weighted residuals for the fits to the model-completed crystal structure (blue), the model generated by SREFLEX where the position of the F(ab) domains was refined (orange), and the GAJOE ensemble fit accounting for multiple conformational states (black). An improved agreement between the model and SAXS data is observed as a smoothing in the residual plots.

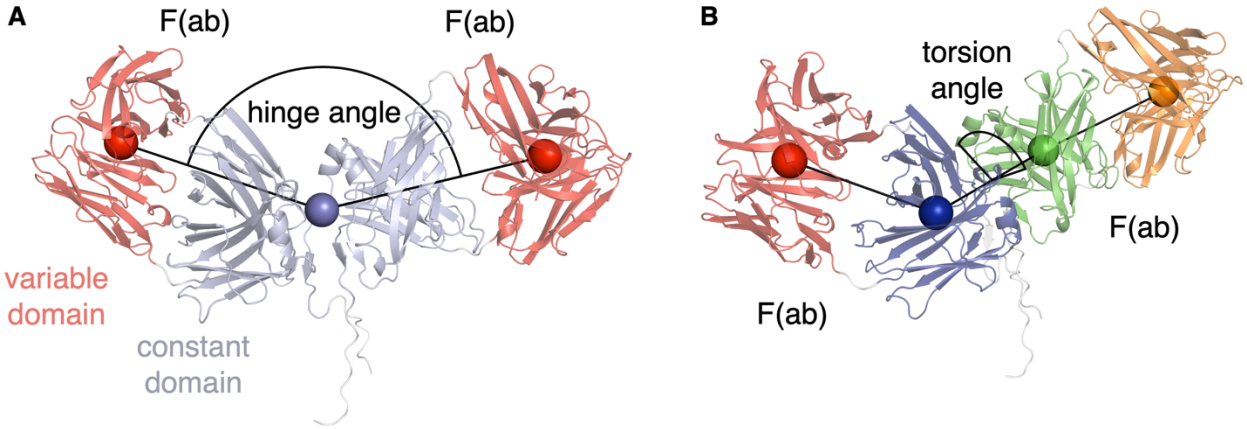

Figure S5. Definition of F(ab)$_2$ hinge and torsion angle. (A) the hinge angle was defined as the angle between the centers of mass of the variable domains (red spheres) and the center of mass of the two constant domains (blue sphere). **(B)** the torsion angle was defined as the rotation between the two F(ab) arms, as measured using the centers of mass of the variable domains (red and orange spheres) and the constant domains (blue and green spheres). For definition of the centers of mass see methods.

	IgG			F(ab)$_2$		
Antibody	**k_a (1/Ms)**	**k_d (1/s)**	**K_D (M)**	**k_a (1/Ms)**	**k_d (1/s)**	**K_D (M)**
ChiLob 7/4 *h*IgG2 (WT)	6.13e+05	3.10e-04	**5.05e-10**	7.00e+05	3.85e-04	**5.49e-10**
C232S+C233S	6.57+e05	4.94e-05	**7.52e-11**	8.64+e05	9.73e-05	**1.13e-10**
C233SκC214S	4.29e+05	4.65e-04	**1.08e-09**	3.68e+05	5.63e-05	**1.53e-09**
C232SκC214S	4.88e+05	4.75e-04	**9.73e-10**	5.40e+-5	5.40e-04	**9.99e-10**

Table S1: Affinity of anti-*h*CD40 ChiLob7/4 *h*IgG2 C/S variants, as IgG and F(ab)$_2$ fragments binding to *h*CD40. The data are derived from SPR analysis as described in methods. Exemplar data shown in **Fig. S1E**.

Kabat	**C233S**	**C232S**	**C233SκC214S**	**C239S**	**C232SκC214S**
Structure	C225S	C224S	C225SκC214S	C228S	C224SκC214S
PDB ENTRY	6TKC	6TKB	6TKF	6TKD	6TKE
agonist activity	-	-/+	+	+++	+++
data collection	Diamond I23	ESRF ID30B	ESRF ID23-1	Diamond I03	Diamond I23
X-ray λ Å	2.76	1.8	1.7	0.98	2.76
space group	P321	$P2_12_12_1$	P321	P321	P321
cell constants a, b, c Å α, β, γ °	149.4, 149.4, 45.8, 90, 90, 120	74.8, 95.1, 150.5 90, 90, 90	149.1, 149.1, 45.8 90, 90, 120	149.1, 149.1, 45.8 90, 90, 120	148.2, 148.2, 45.7 90, 90, 120
resolution Å[a]	74.82 - 2.30 (2.38 - 2.30)	47.64 - 2.00 (2.04 - 2.00)	48.81 - 2.18 (2.25 - 2.18)	128.19 - 1.90 (1.94 - 1.90)	128.35 - 2.35 (2.43 - 2.35)
completeness %[a]	93.6 (85.0)	99.7 (100)	99.9 (98.6)	99.2 (97.4)	99.8 (100)
R_{pim}[a]	0.023 (0.154)	0.018 (0.342)	0.023 (0.394)	0.047 (0.320)	0.077 (0.428)
CC 1/2[a]	0.998 (0.850)	0.999 (0.775)	0.999 (0.762)	0.996 (0.768)	0.985 (0.738)
I/σ(I)[a]	19.0 (4.2)	25.2 (2.3)	25.1 (1.8)	9.4 (2.5)	8.6 (2.2)
multiplicity [a]	40.9 (34.2)	29.5 (27.4)	17.3 (7.1)	6.9 (5.9)	17.9 (19.3)
Wilson B $Å^2$	42.0	36.9	35.7	25.5	51.2
Refinement					
reflections (unique)	1,004,161 (24,537)	2,155,923 (73,149)	529,226 (30,651)	315,242 (45,431)	428,842 (24,021)
R, R_{free} %	18.3, 23.6	18.2, 22.9	19.6, 23.9	17.3, 20.6	19.2, 24.5
average B $Å^2$	49.0	46.0	40.0	30.0	56.0
rmsd bonds Å	0.0141	0.0143	0.0144	0.0153	0.0137
rmsd angles °	1.98	1.94	1.96	1.92	1.93
Ramachandran # (%) preferred, allowed, outlier	392 (94.23) 24 (5.77) 0 (0.0)	841 (97.11) 25 (2.89) 0 (0.0)	407 (96.90) 13 (3.10) 0 (0.0)	416 (98.12) 9 (1.65) 1 (0.23)	393 (94.02) 25 (5.98) 0 (0.0)

Table S2: Crystallographic analysis of anti-*h*CD40 ChiLob7/4 *h*IgG2 C/S F(ab)$_2$ variants. The structures determined in this study are listed ranging by increasing agonist activity as C233S < C232S < C233SκC214S < C239S ≅ C232SκC214S. [a], numbers in parentheses for high resolution bin.

SASBDB	C232S+ C233S SASDLG4	C233S SASDLH4	C232S SASDLF4	C233S κC214S SASDLL4	C239S SASDLJ4	C232S κC214S SASDLK4
Guinier analysis						
R_g (Å)	41.8	40.5	39.6	39.7	40.9	39.9
P(r) analysis						
R_g (Å)	44.4	41.9	41.5	40.5	41.2	41.0
D_{max} (Å)	150.5	145.0	142.0	137.0	134.5	132.5
	Crystal structure fit[b] / rigid body refinement					
PDB	N/A	**6TKC**	**6TKB**	**6TKF**	**6TKD**	**6TKE**
Fit (χ^2)	N/A	13.63	1.89	18.94	4.31	7.53
CorMap p-value	N/A	1.10e-21	0.00037	5.20e-25	2.48e-15	1.11e-21
R_g (Å)	N/A	37.96	38.65	37.65	37.75	37.55
Envelope Ø (Å)	N/A	123.9	127.0	123.8	123.5	122.7
Hinge angle°	N/A	113.87	120.94	115.14	114.91	114.00
Torsion angle°	N/A	62.93	61.35	63.42	63.34	63.40
SREFLEX						
SREFLEX fit (χ^2)	2.09	1.85	1.49	1.45	1.52	1.52
CorMap p-value	0.555	0.006	0.547	0.326	0.179	0.048
R_g (Å)	42.71	41.01	39.77	40.05	40.58	40.21
Envelope Ø (Å)	140.0	132.6	130.7	132.7	133.5	132.7
Hinge angle°	158.9	117.0	124.1	130.1	130.9	126.1
Torsion angle°	141.8	2.7	75.4	85.0	81.5	60.5
GAJOE			**Ensemble fit**			
(χ^2)	2.05	1.71	1.51	1.65	1.52	1.55
CorMap p-value	0.964	0.321	0.999	0.092	0.548	0.047
R_{flex} (random)	~ 93.16 % (~82.26%)	~ 88.39 % (~89.97%)	~ 80.98 % (~86.10%)	~ 83.30 % (~85.85%)	~ 76.33 % (~75.01%)	~ 66.74 % (~78.08%)
R_σ	1.43	0.93	0.89	1.05	2.07	0.81
Ensemble R_g[a] (Å)	43.75	41.94	40.45	40.71	41.01	40.69
Ensemble D_{max}[a] (Å)	144.23	139.70	134.86	137.99	138.81	138.76
Hinge angle°[a]± SD	136.5±16.5	130.7±18.7	127.5±4.5	128.6±1.9	124.4±7.2	130.0±3.4
Variance	271.3	349.3	19.8	3.4	52.1	11.8
Torsion angle°[a]± SD	10.3±91.6	79.4±31.7	48.0±18.8	59.3±12.4	47.8±6.1	69.5±9.2
Variance	8391.1	1002.1	353.4	153.1	37.0	84.8

Table S3: SAXS analysis of anti-*h*CD40 ChiLob7/4 *h*IgG2 C/S F(ab)$_2$ variants. Given are values for R_g and D_{max} determined from Guinier and P(r) analysis, compare methods. SAXS fitting was performed using data cut to q 0.2. PDB coordinates (where available) were fit using Crysol *(1)*. Multi-ensemble fitting used models derived from the atomistic MD using GAJOE (*2*). For ensemble analysis, hinge and torsion angles were calculated from the representative models identified by GAJOE, compare **Fig. S5**. [a], weighted mean. [b]The models of the crystal structures were first completed for amino acids not observed in electron density, before fitting to experimental SAXS data (see Methods). All data were collected at BM29, ESRF, France.